Journal Pre-proof

The effect of the presence of obstacles on the dynamic response of single-degree-of-freedom systems: Study of the scenarios aimed at vibration control

Giulia Stefani, Maurizio De Angelis, Ugo Andreaus

PII: S0022-460X(22)00178-X
DOI: https://doi.org/10.1016/j.jsv.2022.116949
Reference: YJSVI 116949

To appear in: *Journal of Sound and Vibration*

Received date : 27 May 2021
Revised date : 18 December 2021
Accepted date : 11 April 2022

Please cite this article as: G. Stefani, M. De Angelis and U. Andreaus, The effect of the presence of obstacles on the dynamic response of single-degree-of-freedom systems: Study of the scenarios aimed at vibration control, *Journal of Sound and Vibration* (2022), doi: https://doi.org/10.1016/j.jsv.2022.116949.

The effect of the presence of obstacles on the dynamic response of single-degree-of-freedom systems: study of the scenarios aimed at vibration control

Giulia Stefani[a,*], Maurizio De Angelis[a], Ugo Andreaus[a],

[a]*Department of Structural and Geotechnical Engineering, Sapienza University of Rome, Via Eudossiana 18, 00184 Rome, Italy*

Abstract

In this paper, the effect of the presence of (existing or newly added) deformable and dissipative obstacles (bumpers) on the nonlinear dynamic response of a single-degree-of-freedom system, is investigated via parametric numerical analyses. Through the study of possible response scenarios which can occur by varying the bumpers' parameters (i.e., the position, the stiffness, and the damping, respectively) it is observed that the presence of the bumpers is not always unfavorable compared to the free flight condition. By properly selecting the bumpers' parameters it is possible to exploit the occurrence of impacts with beneficial effects. Furthermore, a relationship between the stiffness and the damping parameters of the bumpers, which allows to minimize the maximum value of the mass acceleration in primary resonance condition, is identified and discussed. Although this study is inspired by the practical problem of large horizontal displacements in base-isolated structures, it has a transversal nature with respect to different disciplinary fields. Consequently, the results obtained in this work can be extended also to further applications related to vibro-impact dynamics.

Keywords: vibro-impact dynamics; deformable and dissipative bumpers; nonlinear scenarios; nonlinear vibration control; isolation; parametric numerical study.

1. Introduction

Seismic isolation represents one of the most applied, reliable, and effective, passive control strategies to mitigate the dynamic response of both new and existing structures [1–6], bridges [7–14], strategic facilities [15, 16], nonstructural components and equipment [17–26], works of art [27–29].

Seismically isolated structures, due to the greater flexibility offered by the isolators at the base, are expected to experience large horizontal displacements relative to the ground, especially under near-fault (NF) earthquakes, characterized by long-period pulses [3, 4, 30]. These large displacements, on the one hand, can seriously damage the isolation system by exceeding its limit deformation, on the other, can lead to pounding with surrounding moat walls or adjacent structures if the available seismic gap size is not sufficient. Potential pounding can produce detrimental effects on the effectiveness of seismic isolation and can lead to consequences which range from local slight nonstructural to serious structural damage or even collapse [31–35]. The existence of high spikes in the acceleration response, in correspondence of the floors where pounding occurs, and whose amplitude is influenced by impact rigidity, may affect floor response spectra and thus the response of vulnerable equipment housed in the buildings [36, 37].

To prevent the damage of the isolation system and avoid the occurrence of pounding against adjacent structures, the horizontal displacements can be limited by inserting suitable obstacles, which can be placed at a certain distance (gap) from the structure to be protected (*outer pounding* [38]) or can be incorporated into the isolation system (*inner*

*Corresponding author

Email addresses: giulia.stefani@uniroma1.it (Giulia Stefani), maurizio.deangelis@uniroma1.it (Maurizio De Angelis), ugo.andreaus@uniroma1.it (Ugo Andreaus)

pounding [38]). In the latter case, the built-in buffer (self-braking) mechanism prevents pounding of the isolated structure with the surrounding structures and limits the possible pounding (if any) to be only within the own body of the isolator. Restraining rims are used to limit the motion of the double pendulum sliding bearings experimentally investigated by Bao *et al.* [39]. Harvey *et al.* [40–42] examined the response of double Rolling isolation systems (RISs), in which the motion is limited by the bowl lips acting as hard displacement limits. The roll-n-cage (RNC) isolator introduced by Ismail *et al.* [43–45] incorporates isolation, energy dissipation, buffer, and inherent gravity-based restoring force mechanisms in a single unit. In all these cases the built-in restrainers are quite rigid and impose strict restrains on isolator horizontal displacement once a certain limit value is exceeded.

The occurrence of impact against the obstacles modifies the response of the isolated system, turning it into a nonlinear vibro-impact system. Vibro-impact systems, even the simplest, exhibit complex nonlinear non-smooth dynamics and a wide variety of phenomena (resonances, instabilities, bifurcations, periodic and quasi-periodic trajectories, and chaotic regimes) that need to be carefully investigated [46]. There are several scientific works of both numerical and experimental nature dealing with the nonlinear response of impacting systems. Extremely rich and complex behaviors were observed by Christopher *et al.* [47] in a multi-degree of freedom structure impacting a rigid stop. Costa *et al.* [48] experimentally and numerically explore the complex dynamics of the mass excited impact oscillator presented in Wiercigroch *et al.* [49]. Several interesting behaviors, including period-doubling route to chaos, period-adding cascade, interior and boundary crisis, complete and incomplete chaotic chattering, and different types of bifurcations, were observed by Gritli and Belghith [50] considering a one-degree-of-freedom impact oscillator with a single rigid constraint. Ing *et al.* [51] investigated the behavior of a nearly symmetrical piecewise linear oscillator with flexible constrains, which is a modification of a rig originally designed by Wiercigroch and Sin [52] and examined the bifurcation scenarios close to grazing. The effect of potential asymmetry in the gap and/or stiffness was also investigated. The most complex and interesting behaviors were observed for small clearances, larger forcing amplitude, and for values of the frequency ratio below the natural frequency [52]. The fundamental group of impact motions which can occur in the response of a two-degree-of-freedom system with a clearance and subjected to harmonic excitation were studied by Luo *et al.* [53]. Pattern types, occurrence and stability domains and bifurcation characteristics of periodic motions in a two-degree-of-freedom mechanical impact oscillator with a clearance were investigated by Lyu *et al.* [54]. Considering single and two degree-of-freedom impact oscillators Yin *et al.* [55] discussed the phenomena of coexisting attractors and chaotic transitions including crisis.

Some of the above mentioned behaviors are undesirable as they can cause adverse effects [56]. The study of the behavior of vibro-impact systems, allowing to highlight possible issues associated with the occurrence of impact, is therefore necessary to identify suitable methods to mitigate and control the response of such systems. Several authors proposed different strategies for the control of unstable orbits, bifurcation, co-existing orbits and chaos based on the study of practical problem involving collisions. By using suitable control strategies or by properly selecting the parameters which characterize the vibro-impact problem, it is possible to guide the behavior of the system, to avoid certain scenarios and encourage others, and thus exploit the occurrence of impact with beneficial effects. Wang *et al.* [57] developed a control scheme, named impulsive control method, to stabilize chaotic motions in a class of vibro-impact systems, which consists in implementing the pulses just when the impact occurs. Lenci and Rega [58] proposed to reduce the region of chaotic response of an inverted pendulum with rigid unilateral constraints subjected to a periodic excitation by suitably adjusting the shape of the excitation. The control of multi-stability in a vibro-impact capsule system driven by a harmonic excitation was addressed by Liu and Páez Chávez [59]. The proposed position feedback controller converts the multi-stable capsule system to a bistable one. A position feedback control method, suitable for dealing with chaos control and coexisting attractors, was applied by Liu *et al.* [60] for enhancing the desirable forward and backward capsule motion. Basins of attraction were used to investigate the possibility of switching between coexisting attractors by using the proposed control method. Gritli and Belghith [50, 61] proposed a state-feedback control law to control chaos exhibited by a SDOF impact mechanical oscillator with a single rigid obstacle. A state-feedback controller was designed by Turki *et al.* [62, 63] to stabilize a 1-DoF, periodically forced, impact mechanical oscillator subject to asymmetric two-sided rigid end-stops. Considering two periodically forced oscillators that can interact via soft impacts, Brzeski *et al.* [64] showed that with properly selection of the system's parameters, such as the gap between the systems or/and the phase shift of external excitation, it is possible to decrease the number of coexisting solutions via discontinuous coupling. The results of the analysis carried out by Sun *et al.* [65] showed that by properly designing the dynamic parameters of viscoelastic end-stops, the nonlinear vibration of a SDOF nonlinear suspension system at primary resonance can be effectively suppressed and the jump phenomena can be eliminated for both hardening and softening primary isolators. Furthermore, the end-stop can effectively also attenuate the absolute acceleration response for a hardening primary isolator, while more damping is needed to attenuate that for a softening primary isolator. A two-sided damping constraint control strategy was proposed by Hao *et al.* [66] to improve the performance of the quasi-zero stiffness (QZS) isolator [67]. The proposed control approach can largely lower the isolation frequency while enhancing the effectiveness of isolation in high frequencies and preventing the severity of end-stop impacts. Based on the analysis of two-parameter bifurcations and basins of attraction, the authors found that the key issue to realize such control objective, is the suppression of period-3 solutions that coexist with the desired period-1 orbits.

This paper is part of a research work carried out by the authors and inspired by the practical problem of excessive displacements in base isolated structures. The research concerns the numerical and experimental investigation of the response of a vibro-impact single-degree-of-freedom (SDOF) system limited by two-sided deformable and dissipative obstacles (bumpers) under harmonic base excitation [38, 68–73]. The study concerns the isolation at the base of structures and equipment. The reference isolation system is the one that uses the support of High Damping Rubber Bearings (indicated with the acronym HDRB), the mechanical characteristics of which can be found in [5, 74] with $10-15\%$ damping, but other devices can also be considered, such as friction pendulums, elastoplastic sliding bearings, *etc.* As far as bumpers are concerned, we refer to those made of rubber, whose dissipative capacity depend on the compound, while the stiffness depends not only on the compound but also on the shape of the bumper itself; the identified values of stiffness and damping of the bumpers used in this work refer to the papers [69–71]. The materials with which the damper and the bumpers are constituted are each made with its own compound and therefore each have its own damping, which is partly hysteretic and partly viscous. In this work the dissipative behavior of the damper and the bumpers is modeled by means of an equivalent linear viscous model. Most of previous (experimental and theoretical) studies focused on the nonlinear behavior (scenarios, resonances, . . .) exhibited by the vibro-impact system varying selected parameters [68–73]. In the theoretical-numerical study presented in [68] the authors outlined possible scenarios within the system response. This study guided subsequent experimental laboratory campaigns conducted on a small-scale physical model of the system using the shaking table [69–71]. The study of the scenarios was subsequently resumed and extended, both numerically and experimentally, in [72]. The scenarios observed experimentally were characterized and were reproduced numerically showing a good agreement with the experimental results. Further numerical investigations highlighted the existence of more complex and varied behaviors for gaps smaller than those considered in the experimental tests [72, 73]. The experimental and numerical study presented in [38], compared to the others, dealt with vibration control. The authors highlighted the existence of suitable pairs of bumpers and gaps that allow to reach a trade-off between two conflicting objectives, namely control of excessive displacements and control of excessive accelerations. This goal can be achieved combining small gaps with quite deformable bumpers.

This work represents a deepening and an extension of the study presented in [38]. The aim of the paper is to investigate, through numerical parametric analyses, the effect of the presence of the obstacles (existing or newly added) on the response of the system under harmonic base excitation, compared to the free flight condition, that is without obstacles. Compared to previous works by the authors [72, 73, 75], here the study of the response scenarios which can occur by varying the bumpers' parameters (namely, position, stiffness, and damping, respectively) is directed at vibration control. In particular, the possibility to exploit the occurrence of impact with beneficial effects, by properly selecting the bumpers' parameters, is investigated. Firstly, the effect of forcing frequency and damping factor on the response of a viscously damped SDOF system excited by a harmonic base acceleration will be analyzed through transmissibility and displacement response factor curves in free flight condition (i.e without obstacles). Then, the presence of obstacles will require the effect of dimensionless parameters, namely gap, stiffness, and damping of the obstacles to be taken into account as well and will be studied through parametric numerical analyses, by employing a suitable analytical model and keeping fixed the damping factor of the isolation damper; for several appropriately selected values of dimensionless gap, the response of the system will be studied by varying the dimensionless stiffness of the bumpers and keeping their dimensionless damping fixed. The bumpers decrease - almost always - the displacement, while - unfortunately - the impact increases the acceleration. The conflicting objectives are precisely to reduce displacement without paying a high price in terms of increased acceleration. The purpose of the work is the optimal design, that is to reduce the displacement without excessively increasing the acceleration, reaching an acceptable trade-off. The study of the response scenarios which can occur by varying the bumpers' parameters (specifically, gap and stiffness, and keeping fixed the damping of damper and bumpers) is directed at vibration control, while at the same time wanting to reach the conflicting objective that the displacement be lower compared to the free flight condition. In particular, the possibility to exploit the occurrence of impact with beneficial effects, by properly selecting the bumpers' parameters, is investigated.

The paper is organized as follows. In Sect. 2 the numerical model and the governing equations are presented; in Sect. 3 preliminary considerations on control are made; the results of the numerical simulations are discussed in Sect. 4; the mechanical justification of the condition corresponding to the minimum peak acceleration is given in Sect. 5; finally, the main conclusions and further developments of the work are drawn in Sect. 6.

2. Model and equations of motion

The study was carried out considering a single-degree-of-freedom (SDOF) system (Fig. 1), composed of a mass M (highlighted in green) and an isolation damper (D, highlighted in blue), with two-sided deformable and dissipative bumpers (highlighted in red), denoted as right bumper ($\mathrm{B_R}$) and left bumper ($\mathrm{B_L}$) respectively. The bumpers are symmetrically positioned on both sides of the mass at an initial distance (initial gap) G_{0j} (j = R, L). The damper (D) is modeled by a linear elastic element, with stiffness K, and a linear viscous dashpot, with damping coefficient C, arranged in parallel. The two bumpers are massless and, as the damper, they are modeled by a linear elastic element, with stiffness K_j (j = R, L), and a linear viscous dashpot, with damping coefficient C_j (j = R, L), arranged in parallel. The system is subjected to a harmonic base acceleration $A_\mathrm{t}(t) = A_\mathrm{G} \sin \Omega t$, characterized by amplitude A_G and circular frequency Ω. The relative displacements of the damper and of the bumpers with respect to the ground are denoted as u and u_j (j = R, L) respectively.

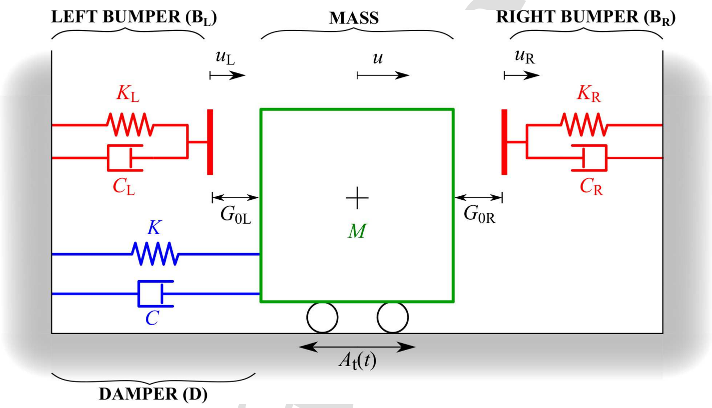

Fig. 1. Model of the SDOF system with two-sided bumpers.

To attempt a more general description of the problem, the equations of motion are written in dimensionless form by introducing the following characteristic quantities [73]: the natural circular frequency of the SDOF system $\omega = \sqrt{K/M}$, the maximum relative displacement $u^* = u_\mathrm{st} R_\mathrm{d,max}$ and the maximum force $F^* = M\omega^2 u^*$ in the SDOF system in free flight (without obstacles) resonance condition. $R_\mathrm{d,max}(\xi) = 1/(2\xi\sqrt{1-\xi^2})$ is the maximum value of the dynamic amplification factor $R_\mathrm{d}(\xi,\beta)$ (Table A.1), defined as the ratio between the amplitude of the dynamic displacement to the static displacement $u_\mathrm{st} = MA_\mathrm{G}/K$.

The following dimensionless quantities were subsequently defined: the dimensionless time $\tau = \omega t$, the dimensionless relative displacements of the mass $q = u/u^*$ and of the bumpers $q_j = u_j/u^*$ (j = R, L), the damping ratio of the SDOF system $\xi = C/(2M\omega)$, the dimensionless amplitude of the base excitation $a_\mathrm{G} = 2\xi\sqrt{1-\xi^2}$, the frequency ratio $\beta = \Omega/\omega$ and the dimensionless gap $\delta_{0j} = G_{0j}/u^*$ (j = R, L). Based on the adopted normalization, for $0 \leq \delta_{0j} < 1$ the mass beats and deforms the j-th bumper, whereas the mass will be in free flight condition (no impact) for $\delta_{0j} \geq 1$. Finally, the generic dimensionless force f was denoted as $f = F/F^*$, where F is its physical value.

By virtue of the above-mentioned dimensionless quantities, the equations of motion of the system can be written in the following dimensionless form:

$$\begin{cases} q''(\tau) + 2\xi q'(\tau) + q(\tau) + f_j(\tau) \cdot \psi_1 \left[\delta_j(\tau)\right] \cdot \psi_2 \left[f_j(\tau)\right] = -a_{\mathrm{G}} \sin\beta\tau & \text{(1a)} \\ f_i(\tau) = 0 & \text{(1b)} \end{cases}$$

where it is assumed that whether $j = \mathrm{L}$ in Eq. (1a), then $i = \mathrm{R}$ in Eq. (1b), or whether $j = \mathrm{R}$ in Eq. (1a), then $i = \mathrm{L}$ in Eq. (1b); in other words, Eq. (1a) governs the motion of the mass in contact with the j−th bumper, while Eq. (1b) refers the free evolution of the i−th bumper; therefore, if the mass is in contact with the right bumper, hence $j = \mathrm{R}$ and $i = \mathrm{L}$, vice-versa if the mass is in contact with the left bumper, hence $j = \mathrm{L}$ and $i = \mathrm{R}$.

In Eq. (1a) the apex ($'$) denotes differentiation with respect to the dimensionless time τ and the Heaviside functions ψ_k $(k = 1, 2)$ are defined as follows:

$$\text{Contact} \quad \psi_1 \left[\delta_j(\tau)\right] = \begin{cases} 0, & \delta_j(\tau) > 0 \\ 1, & \delta_j(\tau) = 0 \end{cases} \tag{2a}$$

$$\text{Separation} \quad \psi_2 \left[f_j(\tau)\right] = \begin{cases} 0, & f_{\mathrm{R}}(\tau) \leq 0 \text{ or } f_{\mathrm{L}}(\tau) \geq 0 \\ 1, & f_{\mathrm{R}}(\tau) > 0 \text{ or } f_{\mathrm{L}}(\tau) < 0 \end{cases} \tag{2b}$$

where $f_j(\tau) = 2\xi\gamma_j q_j'(\tau) + \lambda_j q_j(\tau)$ $(j = \mathrm{R, L})$ is the normalized contact force occurring during the contact period with the j-th bumper, $\gamma_j = C_j/C$ $(j = \mathrm{R, L})$ is the ratio between the viscous damping coefficient of the j-th bumper and that of the damper and $\lambda_j = K_j/K$ $(j = \mathrm{R, L})$ is the ratio between the stiffness of the j-th bumper and that of the damper. $\delta_j(\tau) = \delta_{0j} + \Delta q_j(\tau)$ $(j = \mathrm{R, L})$, where $\Delta q_{\mathrm{R}}(\tau) = q_{\mathrm{R}}(\tau) - q(\tau)$ and $\Delta q_{\mathrm{L}}(\tau) = q(\tau) - q_{\mathrm{L}}(\tau)$, is the clearance function. The latter represents the distance, at each time instant, between the mass and the j-th bumper. When the mass is in contact with the j-th bumper $\delta_j(\tau) = 0$, otherwise $\delta_j(\tau) > 0$.

Despite the relative simplicity of the model, in which both the bumpers and the damper have been modeled with a Kelvin-Voigt model, the system is however strongly nonlinear, due to the presence of clearance, the unilateral constrains and the occurrence of impact that causes abrupt changes of stiffness and damping at the contact time. In the following the model shown in Fig. 1 will be denoted as Simplified Nonlinear Model (SNM).

In this study two equal bumpers symmetrically arranged on the two sides of the mass were considered. Consequently, $\lambda_{\mathrm{R}} = \lambda_{\mathrm{L}} = \lambda$, $\gamma_{\mathrm{R}} = \gamma_{\mathrm{L}} = \gamma$ and $\delta_{0\mathrm{R}} = \delta_{0\mathrm{L}} = \delta_0$.

The equations of motion (Eqs. (1a)-(1b)) were numerically solved using the central difference method [76], implemented with a Matlab code. As concerns the identification of the period in which impact occurs, this was done as follows. The beginning of the contact phase between the mass and the j-th bumper was identified based on the value of the clearance function $\delta_j(\tau)$ $(j = \mathrm{R, L})$, as illustrated in Eq. (2a). Impact occurs when $\delta_j(\tau) = 0$. Regarding instead the evaluation of the time instant of detachment, this was made based on the value of the contact force $f_j(\tau)$ $(j = \mathrm{R, L})$, as illustrated in Eq. (2b). This choice was motivated by the necessity to overcome one of the drawbacks of the Kelvin-Voigt model, when used to model the contact, that is the existence of attracting forces after the restitution phase [77–80]. Since this does not make sense from a physical point of view, in this study the change of sign of the contact force was assumed as indicator of the end of the contact phase.

3. Preliminary considerations

In this section some preliminary considerations on the influence of the involved parameters on the system response (acceleration and displacement) are made, referring to both the situations without and with bumpers. These considerations represent the starting point of the subsequent analyses.

3.1. Without obstacles

In the absence of obstacles (free flight condition, FF) the response of a viscously damped SDOF system excited by a harmonic base acceleration is influenced by the forcing frequency and the damping. The effect of these parameters on the absolute acceleration and relative displacement response of the system can be seen by observing the trend of the transmissibility and the displacement response factor curves as a function of the frequency ratio β and for several values of the damping ratio ξ. In this study, consistently with the normalization adopted in the governing equations

(Sect. 2), both the transmissibility and the displacement response factor were redefined, compared to the classical definition [81]. In particular, in both cases, the normalization was made with respect to the maximum response in resonance condition. The analytical expressions of the transmissibility and the displacement response factor so defined, and denoted as $\mathrm{TR}(\xi,\beta)$ and $R(\xi,\beta)$ respectively, are reported in the lower part of Table A.1 (new definition). The upper part of the same table refers to the classical definition. In Fig. 2, the trends of both $\mathrm{TR}(\xi,\beta)$ (Fig. 2a) and $R(\xi,\beta)$ (Fig. 2b) are plotted as a function of β and for different values of the damping ratio ξ (different colors). The thickness of the line increases with ξ.

Effect of β. Concerning the transmissibility $\mathrm{TR}(\xi,\beta)$ (Fig. 2a), due to the adopted normalization, the assumed value for $\beta = 0$ (highlighted with colored squares) increases with ξ (Table A.1). Increasing β, the transmitted acceleration increases until a maximum is reached for $\beta = \beta_{\mathrm{Ra}}$ (Table A.1), highlighted with colored dots. Due to the adopted normalization the maximum value is equal to unity regardless of damping. By further increasing the frequency ratio β, $\mathrm{TR}(\xi,\beta)$ starts to decrease and tends to zero as $\beta \to \infty$. The maximum transmitted acceleration becomes lower than the ground acceleration, that is $\mathrm{TR}(\xi,\beta) \leq \mathrm{TR}(\xi,0)$, regardless of ξ, for $\beta \geq \sqrt{2}$ (to the right of the colored triangles). Consequently, referring to the transmissibility, this frequency value ($\beta = \sqrt{2}$) divides the frequency interval in two parts:

- for $\beta < \sqrt{2}$ the amplitude of the absolute acceleration transmitted to the mass is greater than the amplitude of ground acceleration, that is $\mathrm{TR}(\xi,\beta) > \mathrm{TR}(\xi,0)$.
- for $\beta > \sqrt{2}$ the amplitude of the absolute acceleration transmitted to the mass is lower than the amplitude of ground acceleration, that is $\mathrm{TR}(\xi,\beta) < \mathrm{TR}(\xi,0)$.

Regarding the displacement response factor $R(\xi,\beta)$ (Fig. 2b), similar considerations apply with some differences. The assumed value for $\beta = 0$ (highlighted with colored squares) increases with ξ if $0 < \xi \leq \sqrt{2}/2$. For $\sqrt{2}/2 \leq \xi < 1$, instead, $R(\xi,0) = 1$. The maximum, equal to one due to the adopted normalization, occurs for $\beta = \beta_{\mathrm{Rd}}$ (Table A.1).

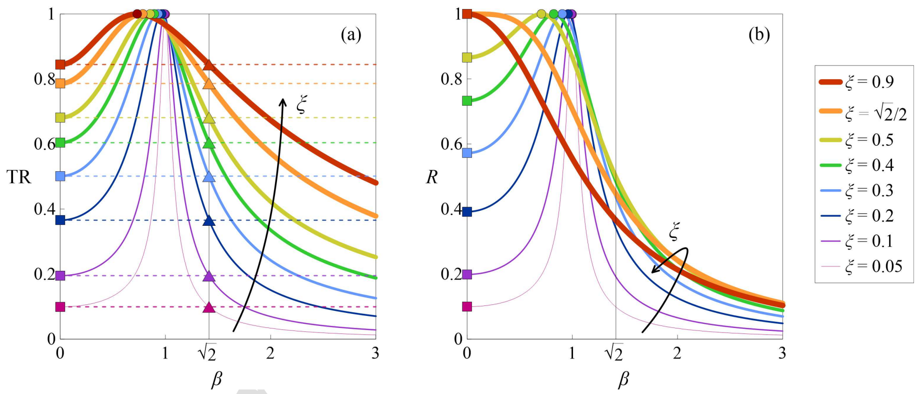

Fig. 2. (a) Transmissibility TR and (b) displacement response factor R for several values of the damping ratio ξ (new definition). The thickness of the line increases with ξ.

Effect of ξ. As concerns the effect of the damping ratio ξ, it reduces the amplitude of motion at all excitation frequencies, particularly in the neighborhood of the resonance. From Fig. 2b, it can be observed that, as ξ increases (for $0 < \xi < \sqrt{2}/2$), while the maximum value of the response in resonance condition (colored dot), always equal to 1, moves to the left, the other points of the curve move upwards both to the left and to the right of the resonance. For $\sqrt{2}/2 \leq \xi < 1$, instead, the maximum value of $R(\xi,\beta)$ is obtained for $\beta = 0$ (colored square). Referring to the transmissibility (Fig. 2a), damping produces opposite effects depending on whether $\beta < \sqrt{2}$ or $\beta > \sqrt{2}$. In particular, for $\beta < \sqrt{2}$ the increase in the damping ratio ξ reduces the maximum transmitted acceleration, whereas for $\beta > \sqrt{2}$ the damping ratio ξ increases the transmitted acceleration. Comparing Figs. 2a and b, it can be observed that for small values of the damping ratio ξ in the neighborhood of the resonance the curves of TR and R are close, both in terms of maximum values and resonant frequencies.

These preliminary considerations give us indications on how, by acting on the damping and frequency ratios (ξ and β), it is possible to mitigate the system response (acceleration and/or displacement) in the absence of obstacles. In particular, the mitigation of the system response can be achieved in two ways: by increasing β for the transmitted acceleration to be less than the ground acceleration (isolation), or by increasing the dissipative capability (increasing ξ) to reduce the dynamic amplification in resonance condition. In the first case the attention is directed towards the frequency interval $\beta > \sqrt{2}$, in which, theoretically, it would be preferable not to have damping; in the second case, instead, the attention is directed towards the frequency interval $\beta < \sqrt{2}$ in which the effect of damping is beneficial.

3.2. With obstacles

The presence of obstacles (existing or newly added) increases the number of parameters that influence the system's response. In addition to the frequency ratio β and the damping ratio ξ, also the effect of the gap δ_0 and of the mechanical properties of the obstacles (λ and γ) must be considered.

For a given value of the dimensionless gap δ_0, it is possible to preliminary identify the frequency interval in which impact surely will occur, based on geometric considerations, as illustrated in [73]. The limits of this frequency interval, denoted as β_1 and β_2 respectively (with $\beta_1 < \beta_2$), can be determined analytically by solving, for each $\xi - \delta_0$ pair, the equation $R(\xi,\beta) = \delta_0$, that is by finding the intersections between the curve representative of the displacement amplification factor $R(\xi,\beta)$, corresponding to the selected ξ value, and the horizontal line $\delta_0 = constant$, as shown in Fig. 3 for $\xi = 0.1$. In this figure, β_1 and β_2 are represented with red and blue dots respectively for some δ_0 values (horizontal dashed lines), and the frequency interval $\beta_1 \leq \beta \leq \beta_2$ is highlighted, for each δ_0, with thick horizontal yellow lines.

The roots of equation $R(\xi,\beta) = \delta_0$ (Table A.1) have the following expressions:

$$- \text{ for } 0 < \xi < \sqrt{2}/2: \begin{cases} \beta_1(\xi,\delta_0) = \sqrt{1 - 2\xi^2 - \dfrac{2\xi}{\delta_0}\sqrt{(\delta_0^2 - 1)(\xi^2 - 1)}} & \text{(3a)} \\ \beta_2(\xi,\delta_0) = \sqrt{1 - 2\xi^2 + \dfrac{2\xi}{\delta_0}\sqrt{(\delta_0^2 - 1)(\xi^2 - 1)}} & \text{(3b)} \end{cases}$$

$$- \text{ for } \sqrt{2}/2 \leq \xi < 1: \begin{cases} \beta_1(\xi,\delta_0) = \sqrt{1 - 2\xi^2 - \dfrac{1}{\delta_0}\sqrt{1 + (2\xi\delta_0)^2(\xi^2 - 1)}} & \text{(4a)} \\ \beta_2(\xi,\delta_0) = \sqrt{1 - 2\xi^2 + \dfrac{1}{\delta_0}\sqrt{1 + (2\xi\delta_0)^2(\xi^2 - 1)}} & \text{(4b)} \end{cases}$$

For a given ξ value (i.e. $\xi = 0.1$), different situations may occur depending on the dimensionless gap δ_0. For $\delta_0 = 1$, that is in free flight (FF) condition, the two roots coincide ($\beta_1 = \beta_2 = \beta_{\mathrm{Rd}}$) and thus impact never occurs for any β value. On the contrary, for $\delta_0 = 0$, that is when the bumpers are initially in contact with the mass, the equation $R(\xi,\beta) = 0$ does not admit roots (Eqs. (3a)-(3b)), and consequently impact occurs for each β value. The interval $0 < \delta_0 < 1$ can be divided into two sub-ranges through the value $\delta_0^* = 2\xi\sqrt{1-\xi^2}$ ($\delta_0^* \simeq 0.199$ for $\xi = 0.1$). For $\delta_0^* < \delta_0 < 1$ (for example $\delta_0 = 0.6$) the two roots β_1 and β_2 are both non null and different from each other, with $\beta_1 < \beta_{\mathrm{Rd}}$ and $\beta_2 > \beta_{\mathrm{Rd}}$. They diverge as δ_0 decreases until, for $\delta_0 = \delta_0^*$, β_1 becomes zero, meaning that impact occurs already starting from $\beta = 0$. For $0 < \delta_0 < \delta_0^*$ (for example $\delta_0 = 0.1$), the equation $R(\xi,\beta) = \delta_0$ admits only one solution (β_2) which increases as δ_0 decreases. Also in this case, impact occurs immediately starting from $\beta = 0$. It is worth noting that impact can occur also outside the frequency range $\beta_1 \leq \beta \leq \beta_2$, depending on the nonlinear behavior of the system, the values of the parameters and the initial conditions, as it will be shown in the following sections.

The introduction of the obstacles changes the response of the system, which will be influenced not only by ξ and β but also by the parameters which characterize the obstacles (position and mechanical properties). Preliminary considerations can already be made based on the position of the obstacle δ_0 (geometrical condition). The response will be further modified considering also the mechanical (stiffness and damping) properties of the obstacles (λ and γ).

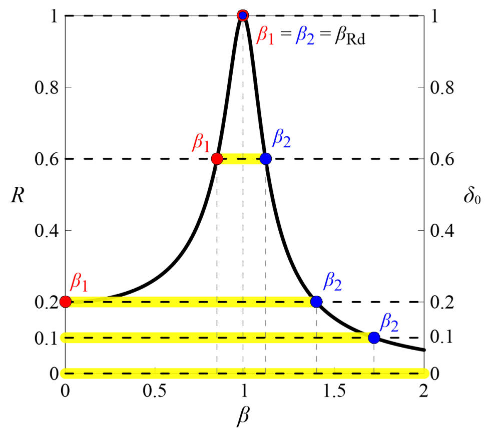

Fig. 3. Dynamic amplification factor R for $\xi = 0.1$ (*thick black curve*) with the location of β_1 (*red dots*) and β_2 (*blue dots*) for some δ_0 values (*horizontal dashed lines*) [73]. For $\beta_1 < \beta < \beta_2$ (*thick horizontal yellow lines*) impact surely occurs for geometric reasons.

Based on these preliminary considerations, it is of interest to investigate the effect of obstacles' parameters (δ_0, λ and γ) on the system response, to identify possible scenarios and make some reasoning on control. The study is carried out numerically assuming a fixed value of the damping ratio $\xi = 0.1$. The curves of the transmissibility TR and of the displacement response factor R, corresponding to $\xi = 0.1$, will be taken as reference curves in the next.

4. Numerical investigations

The effect of the introduction of deformable and dissipative obstacles (bumpers), placed at a certain distance, on the dynamic response of a SDOF system, was studied through parametric numerical analyses, considering the model described in Sect. 2 (SNM) subjected to a stepwise forward and backward sine sweep base excitation.

The study concerns the isolation at the base of structures and equipment. The reference isolation system is the one that uses the support of High Damping Rubber Bearings (indicated with the acronym HDRB), the mechanical characteristics of which can be found in [5, 74] with 10 – 15% damping. The analyses were conducted by assuming $\xi = 0.1$ by way of example and fixing the dissipative capability of the bumpers ($\gamma = 5$). In this section it is shown how the response of the system varies through the introduction of the obstacles, if compared to the free flight condition.

To this aim, the evolution of the forward and backward Pseudo-Resonance-Curves (PRCs) of selected response quantities is traced in terms of the stiffness ratio λ. The response quantities were suitably normalized. The parameter δ_0 varies between 1 in the case of no impact (free flight) and 0 in the case of a bumper positioned adjacent to the mass (pre-contact); in other works by the authors the case of $\delta_0 < 0$ was also considered, i.e. the bumper is pre-stressed and pre-deformed [75], the parameter λ varies between 0 in the case of zero stiffness (i.e. damping constraint) and 100 in the case of very high stiffness compared to that of the isolated system, which produces an impact that can be considered rigid. The parameter γ is chosen equal to 5 because it represents the value identified in the dynamic experimentation on the vibrating table conducted on the isolation damper and on a real bumper [69–71]; it also represents an example case for γ = constant. The damping value, γ, constant, characteristic of the constrained optimization Eq. (6), represents a real situation, as the damping of the rubber bumpers depends on the compound and can be considered known or fixed.

The selected response quantities are: the normalized excursion of the absolute acceleration of the mass $\eta_a = \Delta\alpha/\Delta\alpha_0$, the normalized excursion of the relative displacement of the mass $\eta_d = \Delta q/\Delta q_0$, the normalized excursion of the contact force $\eta_F = \Delta f_B/\Delta\alpha_0$ and the normalized excursion of the deformation of the bumpers $\eta_B = \Delta q_B/\Delta q_0$. The absolute acceleration of the mass $\alpha(\tau)$ is given by the sum of the acceleration of the ground $a_t(\tau) = a_G \sin\beta\tau$ and the relative acceleration between the mass and the ground $q''(\tau)$, that is $\alpha(\tau) = a_t(\tau) + q''(\tau)$. The excursion ($\Delta i$, $i = \alpha,\ q,\ f_B,\ q_B$) was calculated as the difference between the maximum and minimum values recorded at steady state of each sub-frequency range. To calculate the excursion of the contact force (Δf_B) and of the bumpers' deformation (Δq_B), both the bumpers have been considered. Δf_B and Δq_B were calculated as the sum of the maximum absolute values of the contact forces and of the deformations of the two bumpers respectively, recorded at steady state of each sub-frequency range. The normalization was made with respect to the free flight condition. In particular, $\Delta\alpha_0$ and Δq_0 denote the maximum excursion of the absolute acceleration and of the relative displacement of the mass respectively in free flight resonant condition. In addition to these response quantities, also some considerations regarding the resonant frequency of the acceleration β_R and the excursion of the static displacement of the mass $\eta_{d,st}$ will be made.

Starting from the free flight (FF) condition ($\delta_0 = 1$), the investigated δ_0 values were chosen based on the considerations made in Sect. 3, involving vibration isolation and the parameters β_1, β_2, δ_0^*, etc. First, the gap interval $0 \leq \delta_0 \leq 1$ was divided, through the value $\delta_0^* \simeq 0.199$, into two sub-ranges, namely $\delta_0^* \leq \delta_0 \leq 1$ and $0 \leq \delta_0 < \delta_0^*$, to distinguish the situations in which the equation $R(\xi, \beta) = \delta_0$ admits two or one roots. Subsequently, inside these two sub-ranges, some δ_0 values were selected. Referring to the sub-range $\delta_0^* \leq \delta_0 \leq 1$, the following values of the dimensionless gap were selected: $\delta_0 = 1$, $\delta_0 = 0.7$, $\delta_0 = 0.4$ and $\delta_0 = \delta_0^*$. As concerns the sub-range $0 \leq \delta_0 < \delta_0^*$, in addition to the limit value $\delta_0 = 0$, the values of dimensionless gap at which $\beta_2 = \sqrt{2}$ and $\beta_2 = 2$, that is $\delta_0 \simeq 0.1915$ (denoted also as δ_{0c}) and $\delta_0 \simeq 0.066$ respectively, were considered.

4.1. Results

In the following figures (Figs. 4-8) the thick black curves represent the PRCs of η_a and η_d in free flight condition (FF). The other curves represent the forward (solid lines) and backward (dashed lines) PRCs corresponding to increasing values (increasing thickness of the lines) of λ between 0.1 and 100 (the latter assumed conventionally as representative of the impact against a rigid obstacle and denoted as λ_{max}). Only the curves corresponding to some λ values inside this range (namely $\lambda = 0.1, 1, 10, 50, 100$) were represented to make the figures more readable.

As concerns the symbols, the black dots identify the primary resonance condition for all the investigated λ values (even those for which the PRCs are not shown). The yellow squares represent the values of η_a and η_d for $\beta = 0$. The cyan symbols identify the boundaries of the frequency interval in which, for the considered value of δ_0, impact will surely occur, based on purely geometric considerations ($\beta_1 \leq \beta \leq \beta_2$, Sect. 3.2). In particular, the cyan diamond corresponds to β_1 (lower limit of the "geometric" impact range) while the cyan circle corresponds to β_2 (upper limit of the "geometric" impact range). The green triangle was used to represent the β value (denoted as β_c) such that, for $\beta > \beta_c$ the maximum absolute acceleration of the mass is lower than the ground acceleration ($\eta_a < \eta_a|_{\beta=0}$).

Finally, the vertical arrows identify the jumps.

Free flight* ($\boldsymbol{\delta_0 = 1}$)*. For $\delta_0 = 1$ impact does not occur for any β value ($\beta_1 = \beta_2 = \beta_{Rd} \simeq 0.99$) regardless of λ, since the amplitude of the gap is equal to the maximum displacement of the mass in resonance condition. Since in the adopted model (SNM), both the bumpers and the damper were modeled through a linear spring in parallel with a linear viscous dashpot (Kelvin-Voigt model), the corresponding PRCs of η_a and η_d, represented with thick black curves in Figs. 4-8 (FF), coincide with the curves representative of the transmissibility TR and the displacement response factor R for $\xi = 0.1$ (Fig. 2). Due to the considered small value of damping ratio ξ, the PRCs of η_a and η_d in free flight condition are close to each other. Forward and backward curves overlap, without jumps or hysteresis, and the acceleration becomes lower than the ground acceleration for $\beta > \sqrt{2}$.

$\boldsymbol{\delta_0 = 0.7}$. For $\delta_0 = 0.7$ (Fig. 4), impact can occur since β_1 (cyan diamond) and β_2 (cyan circle) (Eqs. (3a)-(3b)) are both different from zero, with $\beta_1 < \beta_{Rd}$ and $\beta_2 > \beta_{Rd}$. In addition to the frequency range in which impact surely occurs, due to geometric considerations ($\beta_1 \leq \beta \leq \beta_2$), the nonlinear behavior of the system causes the occurrence of impact even outside this range.

Due to the hardening caused by the impact, compared to the free flight condition (FF, black curve), the PRCs bend to the right, and the bending becomes more pronounced as the stiffness ratio λ increases. Exceeded a certain value of λ, which will be denoted as λ_H, the system exhibits jump phenomena (highlighted with arrows), leading to the appearance of a hysteresis region between the jumps. The jump phenomena and the hysteresis are observable in the PRCs of both η_a (Fig. 4a), η_d (Fig. 4b), η_F (Fig. 4c) and η_B (Fig. 4d). For the selected value of the dimensionless gap $\lambda_H \simeq 2.2$. As it can be seen from Fig. 4, the frequency value at which the upward jump (blue dashed arrow) occurs, decreasing the forcing frequency (backward sweep), is the same for each λ value and corresponds to β_2. On the contrary, the downward jump (blue solid arrow) occurs, increasing the forcing frequency (forward sweep), at a frequency value, in the following denoted as β_3, which increases with λ. Consequently, β_2 and β_3 give a measure of the extent of the hysteresis region in terms of frequency. As λ increases, this frequency range increases.

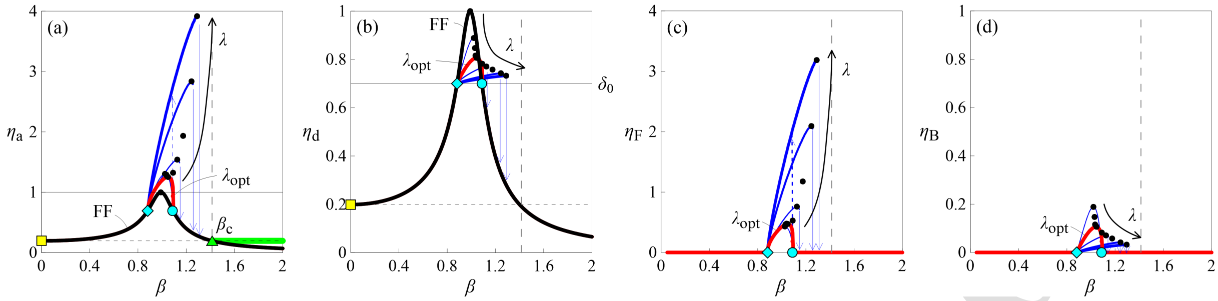

Fig. 4. Sections of the PRCs for $\xi = 0.1$, $\gamma = 5$, $\delta_0 = 0.7$ and for several values of the stiffness ratio λ ($0 < \lambda \leq 100$): (a) η_a; (b) η_d; (c) η_F; (d) η_B. The *black curves* in (a) and (b) represent the free flight (FF) condition, the *red curves* identify the PRCs corresponding to the λ value at which the envelope of the maximum values of the acceleration shows a minimum ($\lambda = \lambda_{opt}$), while the *blue curves* represent the PRCs corresponding to the other values of λ (the thickness of the line increases with λ). The *black dots* identify the primary resonance condition. In (a) and (b) the *yellow squares* indicate the values of η_a and η_d for $\beta = 0$; the *cyan symbols* represent the location of β_1 (*cyan diamond*) and β_2 (*cyan circle*). Finally, in (a) the *green triangle* identifies the β_c value, for all the considered values of λ, such that $\eta_a < \eta_a|_{\beta=0}$ for $\beta > \beta_c$ (*thick horizontal green line*).

In the frequency range corresponding to the hysteresis ($\beta_2 < \beta < \beta_3$), for each β value, and depending on the initial conditions, it is possible to observe two steady-state stable solutions, corresponding respectively to large-amplitude (with impact) and small-amplitude (without impact) oscillations. Actually, there would be also a third unstable solution, that could not be obtained with the used methodology. At the hysteresis region, making a comparison with the free flight condition at the same frequency, the introduction of the obstacle can be counter-productive (occurrence of impact), depending on the initial conditions. It can lead to an increase not only of accelerations, but also of displacements, or, at best, the response does not change (absence of impact). Therefore, the introduction of the obstacle does not always reduce the displacements compared to the free flight condition, as one would expect. Based on these considerations, the hysteresis, if possible, should be avoided (choosing $\lambda < \lambda_H$).

Regarding the primary resonance (highlighted with black dots), it moves to the right, that is it occurs for increasing values of β, as the stiffness ratio λ increases. As concerns the acceleration (Fig. 4a) the maximum value in resonance condition (denoted as η_a^*), starting from the free flight condition (black curve) and increasing λ, first increases, then decreases showing a minimum and subsequently starts to grow again, tending to an almost vertical asymptote for large values of stiffness ratio. For each λ value, the maximum value of η_a is always greater than that corresponding to the free flight condition ($\eta_a^* > 1$). The introduction of the obstacle, on the contrary, always reduces the peak value of the excursion of relative displacement ($\eta_d^* < 1$), and the extent of the reduction increases with λ (Fig. 4b). No changes in the excursion of the static displacement (highlighted with a yellow square) are observed. As concerns the bumpers, both the contact force and the deformation are null in the absence of impact. When impact occurs, the values of the contact force at resonance (black dots in Fig. 4c) show a trend with the stiffness ratio similar to that of the maximum values of the acceleration, with the occurrence of a minimum. The deformation of the bumpers (Fig. 4d), instead, quite small for the selected δ_0 value, always decreases with λ.

From Fig. 4, it can be also noted that, for the considered combination of parameters (ξ, γ and δ_0) and for $0 < \lambda \leq 100$, the occurrence of impact modifies the response of the system only for $\beta < \sqrt{2}$, keeping unaltered the frequency range of interest for the isolation in the linear case, that is $\beta > \sqrt{2}$.

Finally, by looking at the PRCs of η_a (Fig. 4a), it is possible to identify a value of stiffness ratio (denoted as λ_{opt}) for which the envelope of the maximum values of η_a shows a minimum ($\min[\eta_a^*]$), although it is, in any case, $\eta_a^* > 1$. For the considered value of δ_0, this occurs for $\lambda_{opt} \simeq 2$ (thick red curve). In this condition, the resonance occurs for $\beta_R \simeq 1.05$ and since $\lambda_{opt} \simeq 2 < \lambda_H$, no hysteresis is observed. Furthermore, for all the considered values of λ, the acceleration transmitted to the mass becomes smaller than the ground acceleration for $\beta > \sqrt{2}$ (that is $\beta_c = \sqrt{2}$, green triangle). In Fig. 4a this frequency range was highlighted with a horizontal green thick line.

In the condition corresponding to the minimum peak value of η_a ($\lambda = \lambda_{opt}$), also a reduction of the peak value of the relative displacement of the mass, compared to the free flight condition, was noticed (red curve in Fig. 4b). On the other hand, no reduction of the static displacement was observed.

By comparing the PRC corresponding to λ_{opt} (thick red curve) and the PRC in free flight condition (thick black curve) at the same frequency (for $\beta_1 \leq \beta \leq \beta_2$), it can be noted that, in the condition corresponding to the minimum peak value of the acceleration, while the acceleration is always greater than the free flight condition, the displacement is in general lower, except for frequency values slightly lower than β_2, at which the red curve appears to be above the black one.

$\delta_0 = 0.4$. By reducing the dimensionless gap, always remaining in the range $\delta_0^* < \delta_0 < 1$, the amplitude of the frequency interval in which impact occurs increases (Fig. 5, for $\delta_0 = 0.4$). Compared to the previous case ($\delta_0 = 0.7$, Fig. 4), it is possible to identify a value of the stiffness ratio (denoted as $\lambda_c < \lambda_{max}$), beyond which the occurrence of impact modifies the response of the system, compared to the free flight condition, also for $\beta > \sqrt{2}$. For $\delta_0 = 0.4$ this occurs for $\lambda_c \simeq 14$. For $\lambda > \lambda_c$ the transmitted acceleration becomes lower than the ground acceleration after the downward jump, which occurs for increasing values of β as λ increases. Consequently, compared to the linear case, the isolation frequency range decreases.

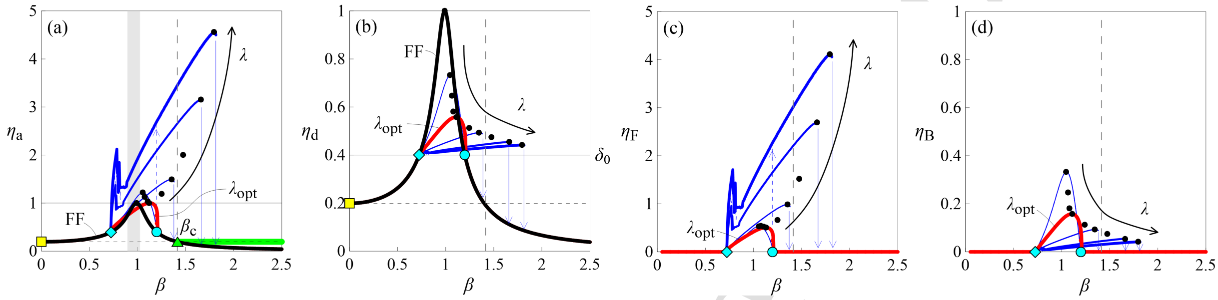

Fig. 5. Sections of the PRCs for $\xi = 0.1$, $\gamma = 5$, $\delta_0 = 0.4$ and for several values of the stiffness ratio λ ($0 < \lambda \leq 100$): (a) η_a; (b) η_d; (c) η_F; (d) η_B. The *black curves* in (a) and (b) represent the free flight (FF) condition, the *red curves* identify the PRCs corresponding to the λ value at which the envelope of the maximum values of the acceleration shows a minimum ($\lambda = \lambda_{opt}$), while the *blue curves* represent the PRCs corresponding to the other values of λ (the thickness of the line increases with λ). The *black dots* identify the primary resonance condition. In (a) and (b) the *yellow squares* indicate the values of η_a and η_d for $\beta = 0$; the *cyan symbols* represent the location of β_1 (*cyan diamond*) and β_2 (*cyan circle*). Finally, in (a) the *green triangle* identifies the β_c value, for $\lambda = \lambda_{opt}$, such that $\eta_a < \eta_a|_{\beta=0}$ for $\beta > \beta_c$ (*thick horizontal green line*). The *vertical gray band* in (a) highlights the frequency interval in which the PRC of η_a corresponding to $\lambda = \lambda_{opt}$ (*red curve*) is below the PRC corresponding to the free flight condition (FF, *black curve*).

Compared to the scenarios observed for $\delta_0 = 0.7$ (Fig. 4), for $\delta_0 = 0.4$, increasing the stiffness ratio, secondary resonances in the low frequency range appear and become gradually evident, affecting increasingly larger frequency ranges. At these secondary resonances, particularly evident in the PRCs of η_a (Fig. 5a) and η_F (Fig. 5c), periodic and quasi-periodic responses can be observed, and the acceleration of the mass appears to be always greater compared to the free flight condition.

As concerns the values of the response in resonance condition (black dots), similar considerations apply to those made for $\delta_0 = 0.7$. Also in this case the envelope of the maximum values of the acceleration, in resonance condition, shows a minimum for $\lambda_{opt} \simeq 1$. Since λ_{opt} is slightly lower than $\lambda_H \simeq 1.2$, no hysteresis occurs. Furthermore, always referring to λ_{opt} (thick red curve), it can be observed that the maximum value of the acceleration in resonance condition, which occurs for $\beta_R \simeq 1.12$, is close to the value corresponding to the free flight condition ($\eta_a^* \simeq 1$). We can see therefore the possibility of reducing the maximum value of the acceleration compared to the free flight condition, also in the presence of impact, by further reducing the dimensionless gap. Furthermore, since $\lambda_{opt} < \lambda_c$, the response of the system is not altered for $\beta > \sqrt{2}$ ($\beta_c = \sqrt{2}$, green triangle in Fig. 5a).

Finally, by comparing the PRC of η_a (Fig. 5a) corresponding to λ_{opt} (thick red curve) and the PRC in free flight condition (thick black curve) at the same frequency (for $\beta_1 \leq \beta \leq \beta_2$), it can be noted that there is a frequency range (highlighted with a vertical gray band) in which, despite the occurrence of impact, the acceleration is lower than in the free flight condition.

$\delta_0 = \delta_0^*$. Moving to the value of the dimensionless gap $\delta_0 = \delta_0^* = 2\xi\sqrt{1-\xi^2} \simeq 0.199$ (Fig. 6), a limit condition is reached in which the impact already occurs for $\beta = 0$ (since $\beta_1 = 0$). In the low frequency range secondary resonances, of different type compared to those observed for $\delta_0 = 0.4$, appear and become gradually evident, affecting increasingly larger frequency ranges as λ increases. In the condition corresponding to the minimum value of the acceleration at resonance (min $[\eta_a^*]$, thick red curve), which occurs for $\lambda_{opt} \simeq 1$, no hysteresis is observed ($\lambda_{opt} < \lambda_H \simeq 1.8$). Since in this condition $\beta_c = \sqrt{2}$ ($\lambda_{opt} < \lambda_c \simeq 2$), the response of the system is not altered for $\beta > \sqrt{2}$, compared to the free flight condition. Furthermore, the maximum value of the acceleration, which occurs for $\beta_R \simeq 1.22$, is lower than the value corresponding to the free flight condition ($\eta_a^* < 1$). Finally, always for $\lambda = \lambda_{opt}$ (thick red curve), it can be noted that, compared to $\delta_0 = 0.4$, the amplitude of the frequency range (highlighted with a vertical gray band) in which, despite the occurrence of impact, the acceleration is lower than in the free flight condition, has increased.

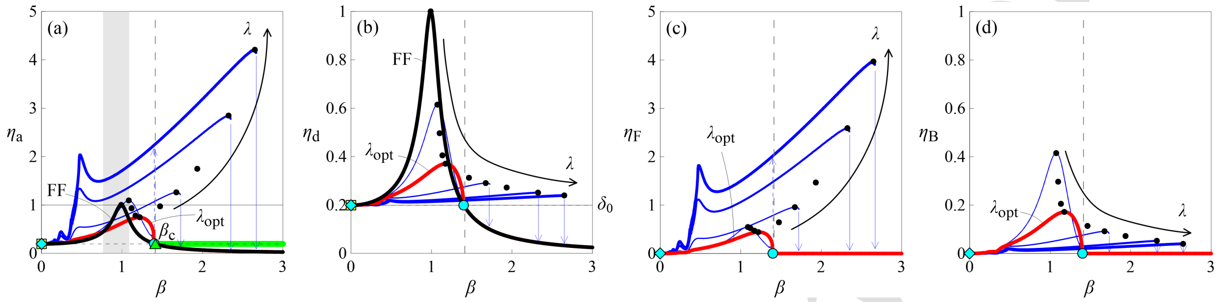

Fig. 6. Sections of the PRCs for $\xi = 0.1$, $\gamma = 5$, $\delta_0 = \delta_0^* \simeq 0.199$ and for several values of the stiffness ratio λ ($0 < \lambda \leq 100$): (a) η_a; (b) η_d; (c) η_F; (d) η_B. The *black curves* in (a) and (b) represent the free flight (FF) condition, the *red curves* identify the PRCs corresponding to the λ value at which the envelope of the maximum values of the acceleration shows a minimum ($\lambda = \lambda_{opt}$), while the *blue curves* represent the PRCs corresponding to the other values of λ (the thickness of the line increases with λ). The *black dots* identify the primary resonance condition. In (a) and (b) the *yellow squares* indicate the values of η_a and η_d for $\beta = 0$; the *cyan symbols* represent the location of β_1 (*cyan diamond*) and β_2 (*cyan circle*). For this value of δ_0 it is $\beta_1 = 0$ and, consequently, the *cyan diamond* is superimposed to the *yellow square*. Finally, in (a) the *green triangle* identifies the β_c value, for $\lambda = \lambda_{opt}$, such that $\eta_a < \eta_a|_{\beta=0}$ for $\beta > \beta_c$ (*thick horizontal green line*). The *vertical gray band* in (a) highlights the frequency interval in which the PRC of η_a corresponding to $\lambda = \lambda_{opt}$ (*red curve*) is below the PRC corresponding to the free flight condition (FF, *black curve*).

$\delta_0 = \delta_{0c}$. By further reducing the gap, the condition in which $\beta_2 = \sqrt{2}$ is reached. Due to the considered damping ratio ξ, the value of dimensionless gap at which this condition occurs, calculated using Eq. (3b) and denoted as δ_{0c}, is slightly lower than δ_0^* ($\delta_{0c} \simeq 0.1915$). The corresponding PRCs are similar to those shown in Fig. 6 and consequently most of the considerations made for $\delta_0 = \delta_0^*$ (Fig. 6) apply also in this case. However, some differences should be highlighted. Since now $0 < \delta_{0c} < \delta_0^*$, the equation $R(\xi,\beta) = \delta_{0c}$ admits only one solution (β_2, cyan circle) and impact occurs already starting from $\beta = 0$. Compared to $\delta_0 = \delta_0^*$, the increase in λ causes a slight decrease also of the static displacement. Finally, for this value of the dimensionless gap $\lambda_H \simeq \lambda_c \simeq 1.8$ and the minimum value of the acceleration in resonance occurs again for $\lambda_{opt} \simeq 1$. In this condition $\eta_a^* < 1$, no hysteresis occurs ($\lambda < \lambda_H$) and, since $\beta_c = \beta_2 = \sqrt{2}$ ($\lambda_{opt} < \lambda_c$), the response of the system is not altered for $\beta > \sqrt{2}$, compared to the free flight condition.

$\delta_0 \simeq 0.066$. Let us now consider the value of the dimensionless gap at which $\beta_2 = 2$, that is $\delta_0 \simeq 0.066$ (Fig. 7). At this δ_0 value, as λ increases, more complex behaviors appear in the low frequency range. Different types of secondary resonances (with left hysteresis or of non-regular type), of a different nature from those observed for greater values of δ_0, appear and become gradually evident, affecting increasingly larger frequency ranges as λ increases. At these secondary resonances, more evident in the PRCs of η_a (Fig. 7a) and η_F (Fig. 7c), both periodic, quasi-periodic and even chaotic solutions can be observed. Furthermore, always at the secondary resonances, the number of impacts between the mass and each bumper, per forcing cycle, is found to increase as β decreases and, for a given β value, as λ increases.

At this δ_0 value, the reduction of the static displacement with increasing λ, already observed for $\delta_0 = \delta_{0c}$, is more evident (yellow squares in Fig. 7b). Compared to δ_{0c}, since in this case $\beta_2 = 2 > \sqrt{2}$, the occurrence of impact modifies, in any case and regardless of λ (with $0 < \lambda \leq 100$), the response of the system also for $\beta > \sqrt{2}$, compared to the free flight condition. The extent of the frequency range affected by such changes does not vary if $\lambda < \lambda_H \simeq 4.4$ (no hysteresis), whereas it becomes gradually larger as λ increases beyond λ_H.

The minimum value of the acceleration in resonance condition occurs for $\lambda_{opt} \simeq 1$. In this condition, since $\lambda_{opt} < \lambda_H$ no hysteresis occurs and furthermore $\beta_c \simeq 1.9$. At resonance, which occurs for $\beta_R \simeq 1.32$, $\eta_a^* < 1$ and,

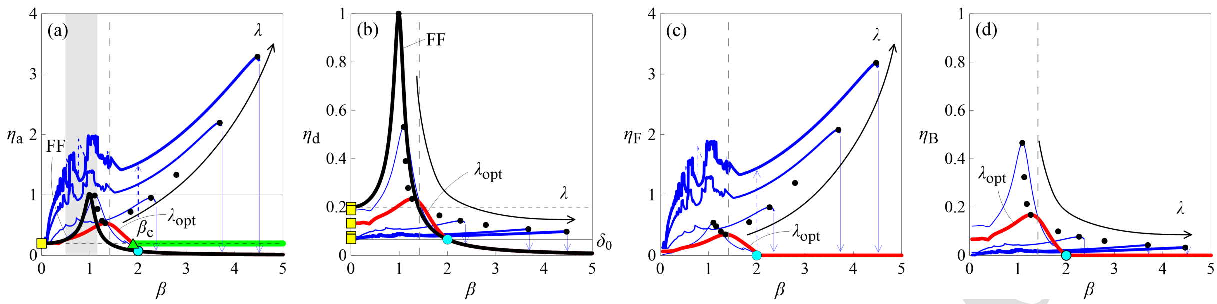

Fig. 7. Sections of the PRCs for $\xi = 0.1$, $\gamma = 5$, $\delta_0 \simeq 0.066$ (value of δ_0 so that $\beta_2 = 2$) and for several values of the stiffness ratio λ ($0 < \lambda \leq 100$): (a) η_{a}; (b) η_{d}; (c) η_{F}; (d) η_{B}. The *black curves* in (a) and (b) represent the free flight (FF) condition, the *red curves* identify the PRCs corresponding to the λ value at which the envelope of the maximum values of the acceleration shows a minimum ($\lambda = \lambda_{\mathrm{opt}}$), while the *blue curves* represent the PRCs corresponding to the other values of λ (the thickness of the line increases with λ). The *black dots* identify the primary resonance condition. In (a) and (b) the *yellow squares* indicate the values of η_{a} and η_{d} for $\beta = 0$. The *cyan circles* represent the location of β_2. Finally, in (a) the *green triangle* identifies the β_{c} value, for $\lambda = \lambda_{\mathrm{opt}}$, such that $\eta_{\mathrm{a}} < \eta_{\mathrm{a}}|_{\beta=0}$ for $\beta > \beta_{\mathrm{c}}$ (*thick horizontal green line*). The *vertical gray band* in (a) highlights the frequency interval in which the PRC of η_{a} corresponding to $\lambda = \lambda_{\mathrm{opt}}$ (*red curve*) is below the PRC corresponding to the free flight condition (FF, *black curve*).

in addition to a substantial reduction of the peak value of acceleration, a noticeable reduction of both the peak value of the displacement and the static displacement is observed. Compared to the previous considered δ_0 values, the amplitude of the frequency range in which, despite the occurrence of impact, the acceleration is lower than in the free flight condition (vertical gray band in Fig. 7a) is increased. However, also the amplitude of the frequency range in which the displacement in presence of impact is greater than in the free flight is increased (Fig. 7b).

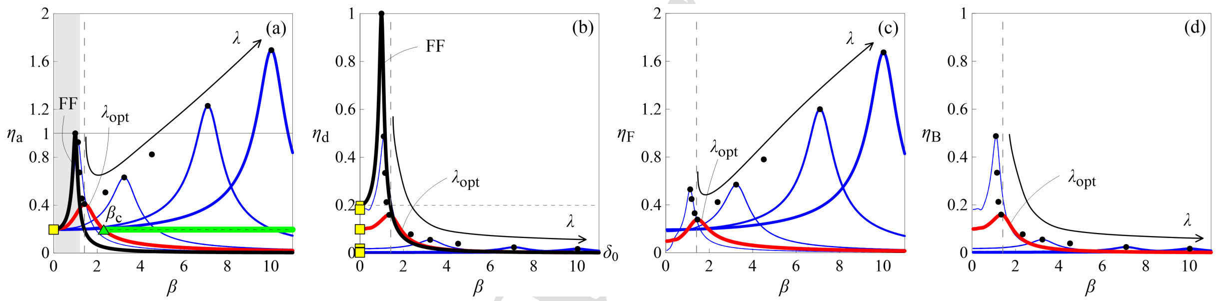

Fig. 8. Sections of the PRCs for $\xi = 0.1$, $\gamma = 5$, $\delta_0 = 0$ and for several values of the stiffness ratio λ ($0 < \lambda \leq 100$): (a) η_{a}; (b) η_{d}; (c) η_{F}; (d) η_{B}. The *black curves* in (a) and (b) represent the free flight (FF) condition, the *red curves* identify the PRCs corresponding to the λ value at which the envelope of the maximum values of the acceleration shows a minimum ($\lambda = \lambda_{\mathrm{opt}}$), while the *blue curves* represent the PRCs corresponding to the other values of λ (the thickness of the line increases with λ). The *black dots* identify the primary resonance condition. In (a) and (b) the *yellow squares* indicate the values of η_{a} and η_{d} for $\beta = 0$. Finally, in (a) the *green triangle* identifies the β_{c} value, for $\lambda = \lambda_{\mathrm{opt}}$, such that $\eta_{\mathrm{a}} < \eta_{\mathrm{a}}|_{\beta=0}$ for $\beta > \beta_{\mathrm{c}}$ (*thick horizontal green line*). The *vertical gray band* in (a) highlights the frequency interval in which the PRC of η_{a} corresponding to $\lambda = \lambda_{\mathrm{opt}}$ (*red curve*) is below the PRC corresponding to the free flight condition (FF, *black curve*).

$\boldsymbol{\delta_0 = 0}$. When the bumpers are initially positioned in contact with the mass ($\delta_0 = 0$) the situation returns to be quite smooth, as shown in Fig. 8, although impact occurs for each β value (Sect. 3.2). Due to the occurrence of impact, the behavior of the system is still nonlinear [72], although the PRCs do not show neither jump phenomena nor hysteresis. As λ increases, the primary resonance moves to higher frequency values, up to about 10 for $\lambda = \lambda_{\max} = 100$. The occurrence of impact modifies, in any case and regardless of λ (with $0 < \lambda \leq 100$), the response of the system for each β value and the PRCs, once exceeded the resonance (black dots), tend to the curve corresponding to the free flight condition (thick black curve) for $\beta \to \infty$. This happens also in the condition corresponding to the minimum peak value of the acceleration ($\lambda = \lambda_{\mathrm{opt}}$, thick red curve), which still occurs for $\lambda_{\mathrm{opt}} \simeq 1$. In this condition, compared to the free flight condition, significant reductions of both the peak value of acceleration, the peak value of the displacement and the static displacement of the mass, are observed. For $\lambda = \lambda_{\mathrm{opt}}$ (thick red curve), the primary resonance occurs for

$\beta_R \simeq \sqrt{2}$ and the acceleration of the mass becomes lower than that of the ground for $\beta > \beta_c \simeq 2.3$.

4.2. Discussion

The study of the evolution of the PRCs with the stiffness ratio λ, for fixed values of both the damping ratios ξ and γ and the dimensionless gap δ_0, allowed to investigate the influence of δ_0, λ and β on the system (mass and bumpers) response. Based on the obtained results, some preliminary conclusions can be drawn.

Scenarios. Starting from the free flight condition ($\delta_0 = 1$) and reducing the gap, gradually more complex scenarios were observed, characterized by the occurrence of a primary hysteresis, secondary resonances of different types in the low frequency range, periodic, quasi-periodic and chaotic responses, multiple impacts, to mention a few. Some of these scenarios do not go in the desired direction thinking of control. However, by properly selecting the bumpers' parameters, it would be possible to guide the system response to reach specific objectives.

Frequency ranges. Starting from $\delta_0 = 1$ and decreasing δ_0, the amplitude of the frequency interval in which impact will surely occur, due only to geometric considerations ($\beta_1 \leq \beta \leq \beta_2$, Sect. 3.2), increases. In Fig. 9, the thick black curve represents the PRC of η_d in free flight (FF) condition. For each δ_0 value (right vertical axis), the extremes of the frequency interval $\beta_1 \leq \beta \leq \beta_2$ are given by the intersections between this PRC and the horizontal line $\delta_0 = constant$. For the considered system and parameters, impact does not occur for $\beta < \beta_1$ (on the left of the ascending branch of the thick black curve in Fig. 9), with β_1 becoming zero when δ_0 reaches the value $\delta_0^* \simeq 0.199$. Furthermore, due to the hardening caused by the impact, when $\lambda > \lambda_H$ (occurrence of hysteresis), where λ_H depends on δ_0, impact can occur also for $\beta_2 < \beta < \beta_3$. β_3 denotes the frequency value at which, during the forward sweep (increasing forcing frequency), the downward jump occurs. In Fig. 9 the blue curves represent the locus of the β_3 values for different stiffness ratios (the thickness of the lines increases with λ).

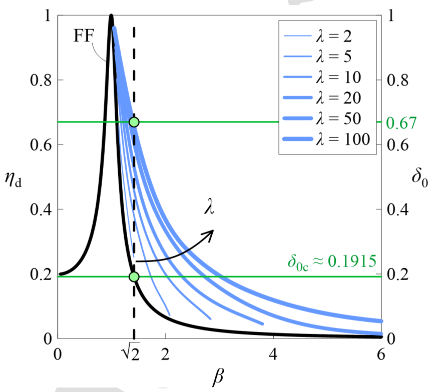

Fig. 9. PRC of η_d in free flight condition for $\xi = 0.1$ (FF, *black curve*) together with the envelopes of the downward jump frequencies (β_3, *blue curves*) for $\gamma = 5$ and several λ values. The thickness of the line increases with λ.

In the two limit cases, namely $\delta_0 = 1$ (free flight condition, absence of impact) and $\delta_0 = 0$ (bumpers initially in contact with the mass, occurrence of impact for each β value) hysteresis never occurs, regardless of λ. For $0 < \delta_0 < 1$, if the horizontal line $\delta_0 = constant$ intersects one of the blue curves, it means that for that pair $\delta_0 - \lambda$ the jump phenomenon, and thus the hysteresis, will occur. The amplitude of the frequency range associated with the hysteresis ($\beta_2 < \beta < \beta_3$, between the descending branch of the black curve and one of the blue curves) increases, for a given δ_0 value, as λ increases (increasing thickness of the blue line) and, for a given λ value, as δ_0 decreases.

From the same figure, it is also possible to see if, for the considered values of δ_0 and λ, due to the occurrence of impact, the response of the system will be modified, compared to the free flight condition, also for $\beta > \sqrt{2}$ (to the right of the vertical dashed line). It depends on the value of β_3. Three gap ranges can be identified. For $\delta_0 > 0.67$ (above the upper horizontal green line) the occurrence of impact will modify the response of the system only in the frequency range $\beta < \sqrt{2}$, for each considered λ value, with $0 < \lambda \leq 100$, since β_3 is always lower than $\sqrt{2}$ (all the blue curves are to the left of the vertical dashed line $\beta = \sqrt{2}$). It is worth noting that the threshold value of the dimensionless gap

$\delta_0 = 0.67$ depends on the maximum value of the stiffness ratio considered in the analysis ($\lambda_{\max} = 100$ in this study) and it increases as $\lambda_{\max}$ increases. For $\delta_0 < \delta_{0c}$ (below the lower horizontal green line), where $\delta_{0c} \simeq 0.1915$ is the value of the dimensionless gap at which $\beta_2 = \sqrt{2}$, the response will be modified in any case, regardless of λ, not only for $0 \leq \beta < \sqrt{2}$, but also for $\beta > \sqrt{2}$. The extent of the frequency range beyond $\sqrt{2}$, affected by the occurrence of impact, becomes gradually larger as λ increases. For $\delta_{0c} \leq \delta_0 \leq 0.67$ (between the two horizontal green lines), the response will be modified also for $\beta > \sqrt{2}$ only if $\lambda > \lambda_c$. For each dimensionless gap within this range, the corresponding λ_c value is that associated with the blue curve which, for the considered δ_0 value, intersects the vertical dashed line $\beta = \sqrt{2}$. It can be observed that λ_c, starting from $\lambda_c = \lambda_{\max} = 100$ for $\delta_0 \simeq 0.67$, decreases as δ_0 decreases.

Resonance condition. For a given δ_0 value, the increase in the stiffness ratio λ causes a gradually more pronounced bending of the PRCs, with the increase in the resonant frequency and the occurrence of the jump phenomena and the hysteresis, for $\lambda > \lambda_H(\delta_0)$. As concerns the values of the selected response quantities in resonance condition (η_i^*, i = a, d, F, B), it was observed that, compared to the free flight condition, the increase in λ causes an increasing reduction of the displacement of the mass and of the deformation of the bumpers, while the acceleration of the mass and the contact force, after a first increase, for very small values of λ, decrease, reach a minimum and then start to grow again. Regarding the static displacement, it decreases, as λ increases, only if $0 \leq \delta_0 < \delta_0^*$.

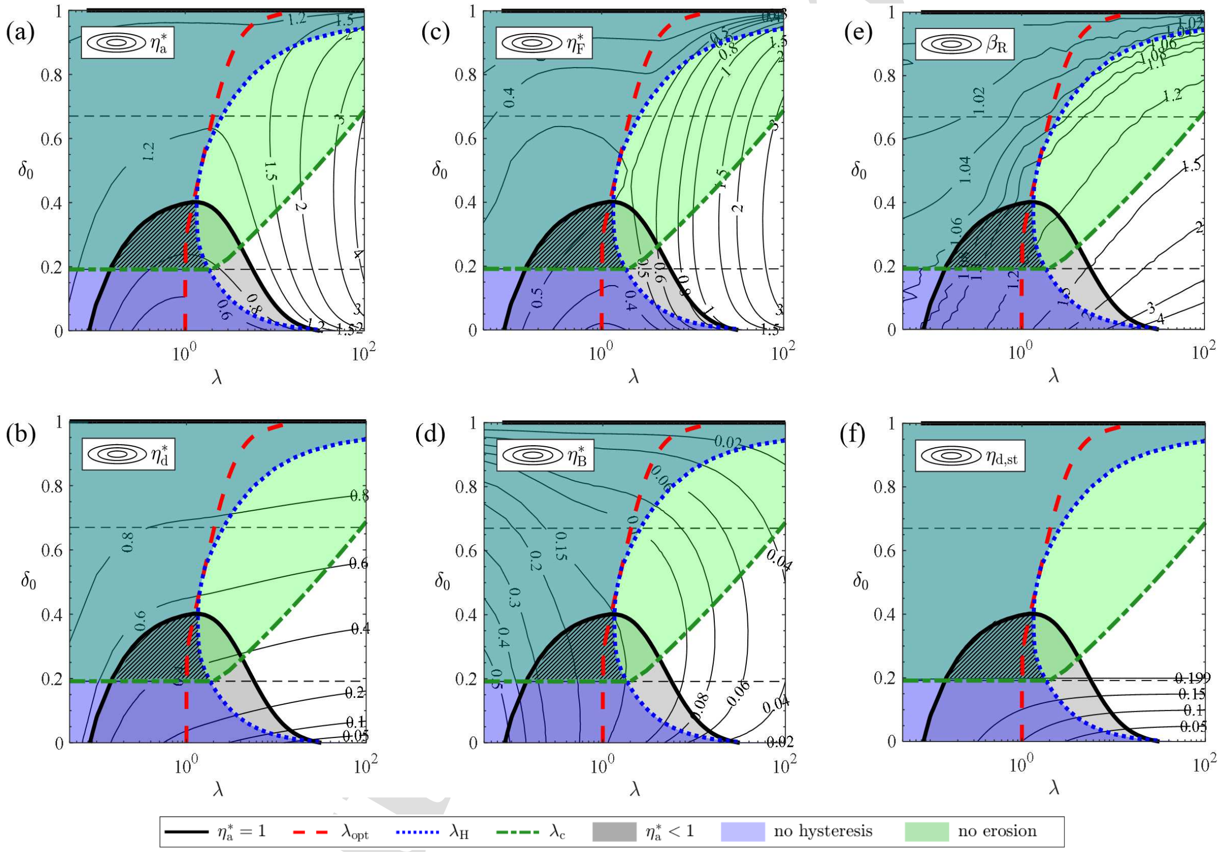

Fig. 10. Contour maps of: (a) η_a^*; (b) η_d^*; (c) η_F^*; (d) η_B^*; (e) β_R; (f) $\eta_{d,st}$ for $\xi = 0.1$, $\gamma = 5$, $0 < \lambda \leq 100$ and $0 \leq \delta_0 \leq 1$. The *solid black curve* highlights the contour level corresponding to a unit value of η_a^*. The *dashed red*, *dotted blue* and *dash-dotted green curves* represent the values of λ_{opt}, λ_H and λ_c respectively, for each δ_0 value. Meaning of the shaded regions: *light gray*: $\eta_a^* < 1$ (between the *solid black curve* and the λ axis); *light blue*: no hysteresis (to the left of the *dotted blue curve*); *light green*: no erosion of the isolation frequency range $\beta > \sqrt{2}$ (above the *dash-dotted green curve*). The *black diagonal hatch* highlights the region of the $\lambda - \delta_0$ plane in which the three shaded areas overlap.

By extending the range of investigation to other values of the dimensionless gap, for $0 \leq \delta_0 \leq 1$ and $0 < \lambda \leq 100$, always assuming $\xi = 0.1$ and $\gamma = 5$, the contour maps shown in Fig. 10 have been obtained. In particular, Figures

10a-d show the contour maps of the maximum values of the excursion of the absolute acceleration of the mass (η_a^*), the relative displacement of the mass (η_d^*), the contact force (η_F^*) and the deformation of the bumpers (η_B^*) respectively. Figs. 10e,f, instead, correspond to the resonant frequency of the acceleration β_R and the excursion of the static displacement $\eta_{d,st}$ respectively. The use of logarithmic scale for the λ axis allows to see better the evolution of the selected quantities in the range of small stiffness ratios.

From Fig. 10a it can be observed that, in most cases ($\lambda - \delta_0$ pairs), the occurrence of the impact against the obstacles causes an increase of the peak value of the acceleration compared to the free flight condition ($\eta_a^* > 1$). For large values of λ, η_a^* can reach values up to 5. However, for small values of λ ($\lambda < 20$) and for $\delta_0 < 0.4$, the peak value of the acceleration, despite the occurrence of impact, can be lower than in free flight condition ($\eta_a^* < 1$). The contour line corresponding to $\eta_a^* = 1$ (solid black curve) divides the $\lambda - \delta_0$ plane in two regions in which $\eta_a^* > 1$ and $\eta_a^* < 1$ respectively. The latter was highlighted with a light gray background.

For each δ_0 value, it is possible to identify the value of λ at which the envelope of the maximum values of the acceleration shows a minimum. The locus of the λ values corresponding to this condition (denoted as λ_{opt}) is represented with a dashed red curve. By focusing the attention on the range $0 \leq \delta_0 \leq 0.4$ at which, through the introduction of the obstacles, it is possible to obtain a reduction of the acceleration, compared to the free flight condition ($\eta_a^* < 1$), it can be observed that the minimum occurs for $\lambda_{opt} \simeq 1$, regardless of δ_0.

The dotted blue curve represents the locus of the values of λ, denoted as λ_H, beyond which, for a given δ_0 value, the jump phenomena, and thus the primary hysteresis, occur. This curve divides the $\lambda - \delta_0$ plane into two regions. To the left of the dashed blue curve no hysteresis occurs (this region was highlighted with a light blue background), whereas to the right there will be the hysteresis. While in the two limit cases ($\delta_0 = 1$ and $\delta_0 = 0$), the hysteresis never occurs, for $0 < \delta_0 < 1$, λ_H decreases as δ_0 decreases, reaching the lower values ($\lambda_H \simeq 1.4$) for $0.3 < \delta_0 < 0.5$, then it starts to increase again as δ_0 further decreases. It can be noted that, for each δ_0 value, $\lambda_{opt} < \lambda_H$ (the dashed red curve is always to the left of the dotted blue curve), meaning that in the condition corresponding to the minimum peak value of the acceleration of the mass ($\lambda = \lambda_{opt}$), the hysteresis never occurs.

Finally, the dash-dotted green curve represents the locus of the values of λ, denoted as λ_c, beyond which, for a given δ_0 value, the occurrence of impact causes a modification of the system response, compared to the free flight condition, also for $\beta > \sqrt{2}$. This curve divides the $\lambda - \delta_0$ plane into two regions. Above the dash-dotted green curve the occurrence of impact will modify the response of the system only in the frequency range $\beta < \sqrt{2}$ (this region was highlighted with a light green background), whereas below the curve also the frequency range $\beta > \sqrt{2}$ will be affected. For $\delta_0 > 0.67$ (upper horizontal dashed line), since there are no intersections between the dash-dotted green curve and the horizontal line $\delta_0 = constant$ (meaning that $\lambda_c > \lambda_{max} = 100$), the response will be modified, due to the occurrence of impact, only in the frequency range $\beta < \sqrt{2}$. On the contrary, for $\delta_0 < \delta_{0c} \simeq 0.1915$ (lower horizontal dashed line) the response will be modified also for $\beta > \sqrt{2}$ regardless of λ. For $\delta_{0c} \leq \delta_0 < 0.67$ (between the two horizontal dashed lines), the isolation frequency range will be reduced, compared to the free flight condition, only if $\lambda > \lambda_c$ (on the right of the dash-dotted green curve).

The curves corresponding to $\eta_a^* = 1$ (solid black curve), λ_{opt} (dashed red curve), λ_H (dotted blue curve) and λ_c (dash-dotted green curve), together with the shaded regions, were reported in all the contour maps in Fig. 10. It can be observed that there is a portion of the $\lambda - \delta_0$ plane that remains white. This means that, for the $\lambda - \delta_0$ pairs belonging to it, $\eta_a^* > 1$, the hysteresis occurs and furthermore the impact causes an erosion of the isolation frequency range $\beta > \sqrt{2}$, compared to the linear case (absence of obstacles). Then there are regions in which only one of the shaded areas exists. Finally, for the other $\lambda - \delta_0$ pairs, two or all the shaded regions can overlap. In particular, the black diagonal hatch highlights the portion of the $\lambda - \delta_0$ plane where all the three shaded areas overlap. This is particularly attractive because, for a $\lambda - \delta_0$ pair inside this region, not only $\eta_a^* < 1$ but also no hysteresis occurs and furthermore the impact does not reduce the isolation frequency range compared to the linear case.

As concerns the peak value of the excursion of the relative displacement of the mass (η_d^*, Fig. 10b), it is always lower than in the free flight condition ($\eta_d^* < 1$). It decreases as δ_0 decreases, for a given λ value, and decreases as λ increases, for a given δ_0 value. In the latter case, the extent of the reduction decreases as λ increases (the contour lines tend to become horizontal).

The contour map of the peak value of the excursion of the contact force (η_F^*, Fig. 10c) is quite similar to that of the acceleration. η_F^* increases with λ, for a given δ_0 value. For a given value of λ, for example $\lambda = 10$, as δ_0 decreases, η_F^* increases, reaches a maximum and then starts to decrease.

As concerns the peak value of the excursion of the deformation of the bumpers (η_B^*, Fig. 10d), it decreases with λ, for a given δ_0 value, becoming particularly small for large values of the stiffness ratio. For a given value of λ, for example $\lambda = 10$, as δ_0 decreases, η_B^* increases, reaches a maximum and then starts to decrease.

As concerns the resonant frequency of the acceleration (β_R, Fig. 10e) it varies between 0.99 and about 10, and the greater values are reached for quite small dimensionless gaps and large values of the stiffness ratio. It increases with λ, for a given δ_0 value, and it increases as δ_0 decreases, for a given λ value.

Finally, regarding the excursion of the static displacement of the mass $\eta_{d,st}$, Fig. 10f shows that for $\delta_0^* \leq \delta_0 \leq 1$ it remains equal to 0.199 independently of δ_0 and λ. On the contrary, for $0 \leq \delta_0 < \delta_0^*$ the static displacement decreases as δ_0 decreases, for a given λ value, and as λ increases, for a given δ_0 value. In the latter case, the extent of the reduction decreases as λ increases (the contour lines tend to become horizontal).

The case $\lambda = \lambda_{opt}$. Let us now focus the attention on the condition corresponding, for each δ_0 value, to the minimum value of the acceleration of the mass in resonance condition. Let us make a section of the contour maps shown in Fig. 10 along the dashed red curve. From Fig. 11a it can be observed that, starting from the free flight condition ($\delta_0 = 1$) and decreasing δ_0, the peak value of the normalized excursion of the absolute acceleration of the mass η_a^* (red curve), starting from a unit value for $\delta_0 = 1$ increases, reaches a maximum for $\delta_0 \simeq 0.8$ ($\eta_a^* \simeq 1.27$) and then starts to decrease, becoming again equal to 1 for $\delta_0 \simeq 0.4$ (vertical dashed line) and lower than 1 for $0 \leq \delta_0 < 0.4$. The minimum value ($\eta_a^* \simeq 0.41$) is reached for $\delta_0 = 0$.

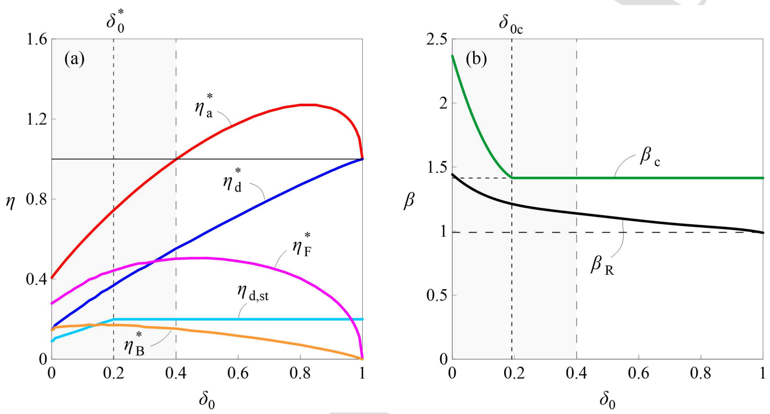

Fig. 11. Trends with the dimensionless gap δ_0 of: (a) values of the system response η_i^* (i = a, d, F, B) at resonance and static displacement of the mass $\eta_{d,st}$, (b) frequency ratios (β_R and β_c), for $\xi = 0.1$, $\gamma = 5$ and $\lambda = \lambda_{opt}(\delta_0)$.

The peak value of the normalized excursion of the relative displacement of the mass η_d^* (blue curve), starting from a unit value for $\delta_0 = 1$, decreases as δ_0 decreases, reaching the minimum value ($\eta_d^* \simeq 0.15$) for $\delta_0 = 0$. As concerns the excursion of the static displacement (light blue curve), it does not vary, remaining equal to $2\xi\sqrt{1-\xi^2} \simeq 0.199$, if $\delta_0^* < \delta_0 \leq 1$, whereas for $0 \leq \delta_0 < \delta_0^*$, it starts to decrease as δ_0 decreases, reaching the value $\eta_{d,st} \simeq 0.09$ for $\delta_0 = 0$.

The peak value of the normalized excursion of the contact force η_F^* (magenta curve), starting from zero for $\delta_0 = 1$ (absence of impact), increases, reaches a maximum for $\delta_0 \simeq 0.45$ ($\eta_F^* \simeq 0.5$) and then starts to decrease, reaching the value $\eta_F^* \simeq 0.28$ for $\delta_0 = 0$. In the gap range of interest ($0 \leq \delta_0 \leq 0.4$, highlighted with a light gray band) η_F^* decreases as δ_0 decreases. The peak value of the normalized excursion of the deformation of the bumpers η_B^* (orange curve), starting from zero for $\delta_0 = 1$ (absence of impact), increases, reaches a maximum for $\delta_0 \simeq 0.15$ ($\eta_B^* \simeq 0.17$) and then slightly decreases, reaching the value $\eta_B^* \simeq \eta_d^* \simeq 0.15$ (the deformation of the bumpers and the displacement of the mass are comparable) for $\delta_0 = 0$. In the gap range of interest ($0 \leq \delta_0 \leq 0.4$, highlighted with a light gray band) η_B^* tends to a constant value as δ_0 decreases.

From Fig. 11b it can be observed that, always for $\lambda = \lambda_{opt}$, the resonant frequency ratio β_R (black curve), starting from $\beta_R \simeq 0.99$ (horizontal dashed line) for $\delta_0 = 1$, increases as δ_0 decreases, reaching the value $\beta_R \simeq 1.47$ for $\delta_0 = 0$. As concerns the β value beyond which the absolute acceleration of the mass is lower than the ground acceleration (β_c, green curve), it is equal to $\sqrt{2}$ if $\delta_{0c} \leq \delta_0 \leq 1$ (the isolation frequency interval is the same as in the linear case), then it starts to increase, reaching the value $\beta_c \simeq 2.37$ for $\delta_0 = 0$. Consequently, for $0 \leq \delta_0 < \delta_{0c}$, as δ_0 decreases, the occurrence of impact causes a greater reduction of the isolation frequency interval, compared to the linear case.

Based on these considerations, although the reduction of the gap allows to reduce the peak value of the response of the system in resonance condition and, for $0 \leq \delta_0 < \delta_0^*$, also the static displacement, very small values of δ_0 involve an increasing modification of the system response in the frequency range of interest for the isolation in the linear case ($\beta > \sqrt{2}$). Consequently, it would be preferable not to reach too low values of δ_0 in order not to alter, or alter to a limited extent, the system response for $\beta > \sqrt{2}$, accepting higher peak values for acceleration, displacement and static displacement of the mass, contact force and deformation of the bumpers.

Other considerations. By comparing, at the same frequency, the PRCs of η_a and η_d for $\lambda = \lambda_{opt}$ with those corresponding to the free flight condition, other interesting considerations have emerged. In general, in the condition corresponding to the minimum value of the acceleration in resonance condition ($\lambda = \lambda_{opt}$), and for $\beta_1 \leq \beta \leq \beta_2$, the displacement is lower compared to the free flight condition, except for a small frequency interval, just before β_2, where the occurrence of impact causes a slight increase of the displacement. As concerns the acceleration, for $0 \leq \delta_0 < 0.4$, there is a frequency range, within $\beta_1 \leq \beta \leq \beta_2$ (highlighted in Figs. 5-8 with a vertical gray band), in which, the acceleration of the mass, despite the occurrence of impact, is lower compared to the free flight condition. As δ_0 decreases, the amplitude of this frequency range increases. Consequently, if the comparison with the free flight condition is made at the same frequency, and not referring to the resonance condition, contrary to what one would expect, the introduction of the obstacle does not always reduce the displacement and does not always increase the acceleration.

5. Mechanical justification of the condition corresponding to the minimum peak acceleration

From the results of the parametric analysis, it was observed that, for each investigated δ_0 value, and for $\xi = 0.1$ and $\gamma = 5$, as λ increases, while the envelopes of the maximum values of the displacement of the mass η_d^* and of the deformation of the bumpers η_B^* decrease, the envelopes of the peak values of the absolute acceleration of the mass η_a^* and of the contact force η_F^* show a minimum. At this condition ($\lambda = \lambda_{opt}$), in addition to the occurrence of the minimum of η_a^* and η_F^*, also a reduction of the peak value of both the relative displacement of the mass and of the deformation of the bumpers was observed. Furthermore, to this is also added the reduction of the static displacement for $0 \leq \delta_0 < \delta_0^*$.

With reference to the range of δ_0 values of greatest interest in this study, that is $0 \leq \delta_0 \leq 0.4$, at which it is possible to obtain a reduction not only of the displacement, but also of the acceleration of the mass, compared to the free flight condition ($\eta_a^* < 1$), it was found that the minimum peak value of acceleration occurs for $\lambda_{opt} \simeq 1$, regardless of δ_0. Based on this observation, the aim of this section is to try to give a mechanical justification to why, for $\xi = 0.1$ and $\gamma = 5$, a unit value of the stiffness ratio λ is preferable to the others.

In the following figures, referring, for illustrative purposes, to the value of the dimensionless gap corresponding to $\beta_2 = 2$ ($\delta_0 \simeq 0.066$), a comparison between different values of stiffness ratio λ is carried out. In addition to the free flight condition (FF), three values of λ were considered, namely the one that corresponds, for the selected δ_0 value, to the minimum of η_a^* ($\lambda = \lambda_{opt} = 1$), and two other values of λ, one lower and the other greater than 1, respectively $\lambda = 0.1 < \lambda_{opt}$ and $\lambda = 5 > \lambda_{opt}$.

In Fig. 12 the comparison between the different λ values is made in terms of force-displacement cycles in resonance condition. Figure 12a refers to the mass (inertia force f_I vs. relative displacement q of the mass), whereas Fig. 12b refers to the bumpers (contact force f_j vs. position d_j of the bumper, j = R, L). The position of the extremity of the bumper, measured from the side of the mass at time $\tau = 0$, is related to its deformation q_j through the expression $d_j(\tau) = q_j(\tau) + \delta_{0j}$ (j = R, L). Starting from zero initial condition, the thin lines represent the transient response, while the cycles at steady state are highlighted with thicker lines. The gray curve refers to the free flight condition (FF), the blue curve to $\lambda = 0.1$, the red curve to $\lambda = \lambda_{opt} = 1$ and the black curve to $\lambda = 5$. The two black dashed vertical lines represent the initial position of the bumpers (initial gap δ_0).

In Fig. 13 the comparison is made in terms of time histories (first 10 cycles), starting from zero initial conditions. The first column (Figs. 13a, d, g) refers to $\lambda = 0.1$, the second (Figs. 13b, e, h) to $\lambda = 1$ and the third (Figs. 13c, f, i) to $\lambda = 5$. In Figs. 13a-c the gray line and the black line represent the position $d(\tau)$ of the mass (which is nothing more than its displacement relative to the ground $d(\tau) = q(\tau)$) in free flight condition (FF, gray line) and after

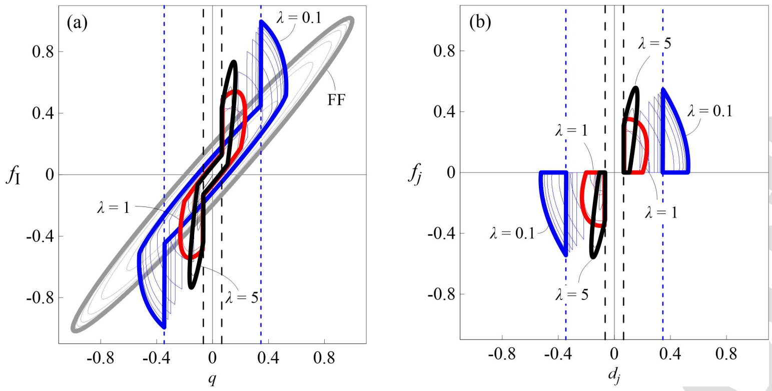

Fig. 12. Force-displacement cycles (ξ = 0.1, γ = 5, $\delta_0 \simeq$ 0.066) in resonance condition ($\beta = \beta_R(\lambda)$), without obstacles (free flight FF, $\beta_R \simeq$ 0.99, *gray line*), and for three values of the stiffness ratio, namely λ = 0.1 ($\beta_R \simeq$ 1.1, *blue line*), λ = 1 ($\beta_R \simeq$ 1.32, *red line*) and λ = 5 ($\beta_R \simeq$ 1.85, *black line*): (a) mass; (b) bumpers. Starting from zero initial conditions, the thin lines represent the transient response, while the thick lines highlight the cycle at steady state.

the introduction of the obstacles (black line). The red and blue lines represent the position of the extremity of the right (B_R) and left (B_L) bumper respectively. In Figs. 13d-f the gray line and the black line represent the absolute acceleration $\alpha(\tau)$ of the mass in free flight condition (FF, gray line) and after the introduction of the obstacles (black line). Finally, Figs. 13g-i show the time histories of the contact forces $f_j(\tau)$ (j = R, L) between the mass and the right (B_R, red line) and left (B_L, blue line) bumper, respectively.

From Fig. 12a it can be observed that, compared to the free flight condition (FF, gray curve), the introduction of gradually stiffer obstacles (increasing λ), keeping fixed the gap δ_0, results in a gradually increasing reduction of the maximum displacement of the mass, while the peak value of the inertia force (and thus of the absolute acceleration of the mass) shows a minimum for λ = 1 (red curve) and then it starts to increase. As concerns the bumpers (Fig. 12b), the increase in λ causes a reduction of the deformation of the bumpers, while the peak value of the contact force shows a minimum for λ = 1 and then it starts to increase. Furthermore, it can be noted that, compared to λ = 1 (red cycle) and λ = 5 (black cycle), for λ = 0.1 (blue cycle), as time goes by, the distance between the mass and the bumpers (gap) gradually increases, reaching, at steady state, a value greater than the initial one ($\delta_{0,\mathrm{fin}} \simeq 0.34 > \delta_0$, represented with blue dotted vertical lines in Figs. 12a,b).

As it can be seen from Fig. 13a, for λ = 0.1, the mass impacts the bumper before the complete recovery of its deformation, causing the impact to occur, for each forcing cycle, for a value of the gap gradually greater than the initial one (horizontal dashed lines), reaching the final value of about 0.34 at the steady state. This behavior is due to the relatively large value of the relaxation time of the bumpers, that is the time the bumper needs to completely recover its deformation, which depends on its dissipative capabilities. It is defined as:

$$\tau_{rj} = \omega \frac{C_j}{K_j} = 2\xi \frac{\gamma_j}{\lambda_j} \quad (j = \mathrm{R,\ L}) \tag{5}$$

For a fully elastic material (γ_j = 0) τ_{rj} = 0 (j = R, L), and so the recovery is instantaneous, whereas a fully viscous material (λ_j = 0) $\tau_{rj} \to \infty$ (j = R, L) remains deformed after the detachment, without recovering its deformation. In presence of both elastic and viscous components, the relaxation time is finite and depends on the dissipative capability of the material. For ξ = 0.1, γ = 5 and λ = 0.1 it is τ_{rj} = 10 (j = R, L). The bumper does not have enough time to completely recover its deformation, and thus to dissipate all the stored energy during the contact, before the mass impacts it again. Consequently, when impact occurs it has a residual deformation, which causes the actual gap to be greater than the initial one (δ_0).

For λ = 5 (Fig. 13c), on the contrary, the bumper quickly recovers the deformation after the detachment from the mass (τ_{rj} = 0.2, j = R, L) and it remains, for a certain time, in the undeformed configuration until the mass impacts it again.

For λ = 1 (Fig. 13b), instead, the mass impacts the bumper practically at the time instant when it has finished recovering all its deformation. Consequently, the bumper has enough time to recover, and, at the same time, it does

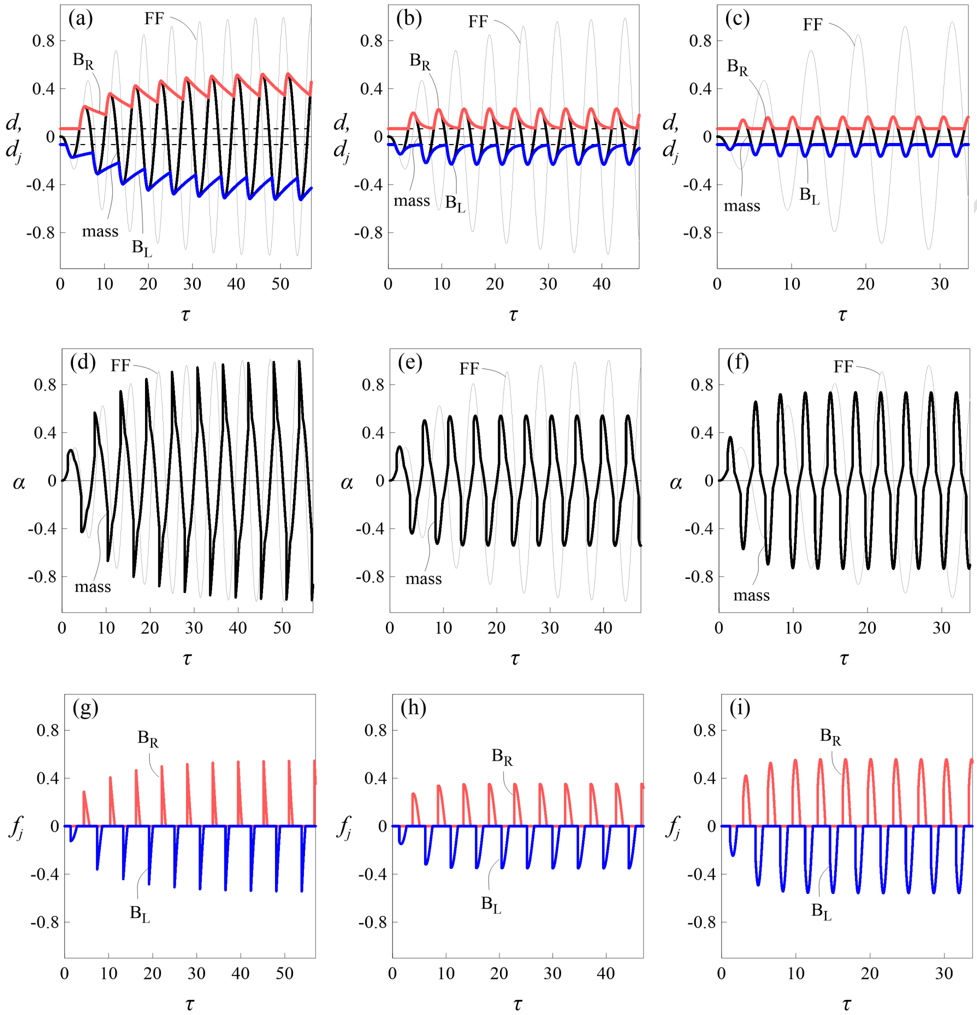

Fig. 13. Time histories of the first ten cycles of the response starting from zero initial conditions, for $\xi = 0.1$, $\gamma = 5$, $\delta_0 \simeq 0.066$. Position of the mass (*black line*) and the bumpers (*red line* for the right bumper B_R and *blue line* for the left bumper B_L): (a) $\lambda = 0.1, \beta_R \simeq 1.1$; (b) $\lambda = 1, \beta_R \simeq 1.32$; (c) $\lambda = 5, \beta_R \simeq 1.85$. Absolute acceleration of the mass (*black line*): (d) $\lambda = 0.1, \beta_R \simeq 1.1$; (e) $\lambda = 1, \beta_R \simeq 1.32$; (f) $\lambda = 5, \beta_R \simeq 1.85$. Contact force between the mass and the bumpers (*red line* for the right bumper B_R and *blue line* for the left bumper B_L): (g) $\lambda = 0.1, \beta_R \simeq 1.1$; (h) $\lambda = 1, \beta_R \simeq 1.32$; (i) $\lambda = 5, \beta_R \simeq 1.85$. In (a)-(f) the *gray line* represents the response (position and absolute acceleration) of the mass in free flight (FF) condition (without obstacles).

not remain inactive. For $\xi = 0.1$ and $\gamma = 5$, this value of λ corresponds to an approximately unit value of the dimensionless relaxation time ($\tau_{rj} = 1$, $j = \mathrm{R, L}$).

From the time histories of the absolute acceleration of the mass (Figs. 13d-f) it is possible to observe the spikes due to the occurrence of impact. Furthermore, as concerns the amplitude of the acceleration after the introduction of the obstacle (black curve), it can be noted that for $\lambda = 0.1$ (Fig. 13d) it is comparable with that corresponding to the free flight condition, while for the other two values of stiffness ratio, it is lower. In particular, for $\lambda = 1$, the reduction is greater, as already observed by looking at the force-displacement cycles (Fig. 12a). At the value of the stiffness ratio corresponding to the minimum of the peak value of the acceleration, also a minimum of the peak value of the contact force corresponds, as shown in Fig. 13h.

Based on these considerations, it would seem that, for a given δ_0 value, for $0 \leq \delta_0 \leq 0.4$, and for $\xi = 0.1$ and $\gamma = 5$, when the stiffness ratio is such that the dimensionless relaxation time is close to unity ($\tau_{rj} \simeq 1$, $j = \mathrm{R, L}$), the maximum value of the acceleration of the mass η_a^* reaches a minimum. This is probably due to the fact that the bumpers are fully exploited, meaning with this that they have enough time to recover their deformation by dissipating energy and, on the other hand, they do not remain inactive because impact practically occurs immediately after recovery. Consequently, for $\xi = 0.1$, $\gamma = 5$ and $0 \leq \delta_0 \leq 0.4$, the condition $\tau_{rj} \simeq 1$ (j = R, L) can be reasonably assumed as representative of the condition which corresponds to the minimum value of the acceleration of the mass in resonance condition. This allows to reduce the number of parameters which characterize the obstacles (position δ_0, and mechanical properties γ and λ), since two of them (γ and λ) are related to each other through the relationship:

$$\frac{\gamma_j}{\lambda_j} \simeq \frac{1}{2\xi} \quad (j = \mathrm{R},\ \mathrm{L}) \tag{6}$$

6. Conclusions

In this paper, the effect of the presence of deformable and dissipative obstacles (bumpers), existing or newly added, on the nonlinear dynamic response of a base excited SDOF system was investigated through numerical parametric analyses. The study of the nonlinear dynamic behavior of the system is necessary to get some indications on how to guide the system response to reach specific objectives, albeit conflicting ones. In fact, this study was inspired by the practical problem of large horizontal displacements in base-isolated structures, the limitation of which can cause unwanted and dangerous increases in the acceleration peak.

The selected response quantities are absolute acceleration and relative displacement of the mass, contact force and deformation of the bumpers, resonant frequency of the system, static displacement of the mass.

Some general conclusions can be preliminary established:

- The parametric study allowed to highlight possible scenarios, characterized by the occurrence of primary hysteresis, secondary resonances of different types in the low frequency range, periodic, quasi-periodic and chaotic responses, multiple impacts, to mention a few, that may be encountered due to the occurrence of impact, varying the obstacle's parameters (position and mechanical properties).

- As part of the control, while some of these scenarios (for example jumps and hysteresis, secondary resonances at low frequencies, coexistence of multiple solutions) do not go in the desired direction, others are desirable (displacements and acceleration with obstacles smaller than those ones in free flight).

- By properly selecting the bumpers' parameters it is possible to guide the system's response to reach specific objectives, avoiding some undesirable scenarios and encouraging others, and thus exploiting the occurrence of impact with beneficial effects.

By fixing the value of the damping factor ξ of the isolation damper and the dissipative capabilities γ of the bumpers (in this work exemplary values $\xi = 10\%$ and $\gamma = 5$ were assumed), the results showed that the occurrence of the impact against the bumpers can significantly modify the system response, depending on the values of the dimensionless gap and of the stiffness ratio, both for $\beta < \sqrt{2}$ (isolation not effective in the linear behavior) and $\beta > \sqrt{2}$ (isolation effective in the linear behavior). The value $\sqrt{2}$ is decisive in the case of linear behavior, because it is the separation value between the frequency interval in which the isolation is not effective ($\beta < \sqrt{2}$) and the frequency interval in which the isolation is effective ($\beta > \sqrt{2}$).

While the peak value of the displacement of the mass is always reduced compared to the free flight condition, the peak value of the acceleration in general is increased, except for small values of both the stiffness ratio ($0.2 \leq \lambda \leq 8$, around the optimal value $\lambda_{opt} = 1$, see the solid black curve in Fig. 10) and the dimensionless gap ($0 \leq \delta_0 \leq 0.4$, see Fig. 10), for which the peak acceleration can be lower compared to the free flight condition.

It is worth noting that, when the comparison with the free flight condition is made at the same frequency, and not comparing the values at the primary resonance, there could be a small frequency interval where the occurrence of impact can cause a slight increase of the displacement, contrary to what is expected. With reference to the exemplary case $\xi = 0.1$ and $\gamma = 5$, and with reference to Figs. 5b-8b, this phenomenon begins at $\delta_0 = 0.4$ with $1.2 \leq \beta \leq 1.25$ (Fig. 5b), when the red optimality curve (denoted with the symbol λ_{opt}) begins to fall below the black curve of free flight (FF), in the interval in which the control achieved through the impact is beneficial, and arrives at $\delta_0 = 0$ with $1.3 \leq \beta \leq 4$ (Fig. 8b); as δ_0 decreases, the far right grows little compared to unit value, while the far left goes to zero. The abovementioned phenomenon of the so called *"bouncing"* extends both to the right and to the left on the β abscissa axis; in the absence of control this phenomenon acquires relevance, while control attenuates its intensity. Equally, there could be a small frequency interval where the occurrence of impact can cause a decrease of the acceleration, compared to the absence of obstacles. With reference to Figs. 5a-8a, such an interval starts from $0.9 \leq \beta \leq 1.1$ at $\delta_0 = 0.4$ (Fig. 5a) and reaches $0 \leq \beta \leq 1.2$ at $\delta_0 = 0$ (Fig. 8a).

It was observed that, for each value of the dimensionless gap, inside the range of interest, it is possible to identify a condition preferable to the others at which the envelope of the values of the acceleration in resonance condition shows a minimum. This occurs, regardless of the dimensionless gap, when the stiffness ratio and the damping ratio, which define the mechanical properties of the bumpers, are such that the relaxation time τ_r is about 1. In this condition the bumpers, on the one hand, have enough time to recover their deformation, after the detachment from the mass, by dissipating energy and, on the other, they do not remain inactive because impact practically occurs immediately after recovery. Consequently, two important conclusions can be drawn, at least limited to the situations explored with the parametric survey carried out here:

- For $\xi = 0.1$, $\gamma = 5$ and, the condition $\tau_r \simeq 1$ can be reasonably assumed as representative of the condition which corresponds to the minimum value of the acceleration of the mass in resonance condition. In addition, the dimensionless acceleration becomes less than unity in the range $0 \leq \delta_0 \leq 0.4$.

- This allows to reduce the number of parameters which characterize the obstacles (position δ_0, and mechanical properties γ and λ), since two of them, namely γ and λ, are related to each other through the relationship: $\gamma/\lambda \simeq 1/(2\xi)$.

In the condition corresponding to the minimum value of the acceleration in resonance neither jumps nor hysteresis occur, and in addition to the minimum value of the acceleration in resonance condition, also a significant reduction of the displacement was observed. In Fig. 11 left, the dimensionless displacement decreases almost linearly from a value of 1 for $\delta_0 = 1$ to a value of 0.18 for $\delta_0 = 0$. To this is also added the reduction of the dimensionless static displacement for small gaps; it maintains the constant value 0.2 ($\simeq \delta_0^*$) in the range $\delta_0^* \leq \delta_0 \leq 1$ and decreases linearly to the value 0.1 in the range $0 \leq \delta_0 \leq \delta_0^*$. The results of Fig. 11 left also showed the trends of the system's response in resonance condition as the dimensionless gap decreases. The dimensionless acceleration first starts from the unitary value at $\delta_0 = 1$, rises to the value 1.3 for $\delta_0 = 0.8$ touching the maximum, drops to 1 for $\delta_0 = 0.4$ and reaches the minimum value 0.4 for $\delta_0 = 0$. The dimensionless displacement starts from the unitary value for $\delta_0 = 1$ and decreases almost linearly up to the value 0.2 for $\delta_0 = 0$. The dimensionless contact force starts from the zero value for $\delta_0 = 1$, attains the maximum value 0.5 for $\delta_0 = 0.4$, and then falls to the value 0.3 for $\delta_0 = 0$. The dimensionless static displacement starts from 0.2 for $\delta_0 = 1$, remains constant up to $\delta_0 = 0.2$ ($\simeq \delta_0^*$), and then goes down almost linearly up to the value 0.1 for $\delta_0 = 0$. Furthermore, the results of Fig. 11 right showed that the resonant frequency ratio starts from the unit value for $\delta_0 = 1$, grows almost linearly up to the value 1.25 for $\delta_0 = \delta_{0c} = 0.2$, and then rises to the value 1.5 for $\delta_0 = 0$ with a slightly greater slope.

However, very small values of δ_0 involve an increasing modification of the system response in the frequency range of interest for the isolation in the linear case ($\beta > \sqrt{2}$). In fact, up to $\delta_0 \geq 0.2 = \delta_{0c}$ there is no erosion, being δ_{0c} the separation value between the effective and non-effective range of the isolation in the linear field. Below the value $\delta_0 = 0.2$, the isolation zone begins to be eroded, up to $\beta_c = 2.5$ for $\delta_0 = 0$; therefore, the zone of effectiveness is eroded because it exists only for β values greater than $\beta_c = 2.5$. For the above reason, that is in order not to alter, or alter to a limited extent, the system response in the effective range of isolation, it would be preferable not to reach too low values of δ_0, accepting slightly higher peak values of the response in terms of acceleration and displacement. A reasonable suggestion could be to stay below $\delta_0 = 0.4$ to have dimensionless acceleration and displacement less than 1 and for example choose $\delta_0 = 0.2$, thus obtaining $\eta_a^* = 0.8$ and $\eta_d^* = 0.4$.

Regarding to the future developments of this work, there is the intention to exploit the obtained results to give guidance on the optimal design of the bumpers.

Declaration of Competing Interest

The authors declare that they have no conflict of interest.

Acknowledgements

This work was partially funded by Sapienza University of Rome [grant numbers RG11916B8160BCCC, RM11715C8262BE71 and RM11715C7CE6AAA6].

Appendix A. Analytical expressions of transmissibility and displacement response factor according to the new definition

The following Table A.1 provides the analytical expressions of the transmissibility (left column) and of the displacement response factor (right column), referring to both the classical (upper part) and the new (lower part) definitions. In addition, also the analytical expressions and/or the values they assume for $\beta = 0$ and in resonance condition, are shown, together with the expressions of the resonant frequency. The given expressions for β_{Rd}, $R_{\mathrm{d,max}}$, and R are valid for $0 < \xi < \sqrt{2}/2$. For $\sqrt{2}/2 \leq \xi < 1$, no peaks occur for R_{d} and the maximum response occurs for $\beta = 0$ and, consequently, $R_{\mathrm{d,max}} = 1$. It follows that, for $\sqrt{2}/2 \leq \xi < 1$, $R(\xi, \beta) = 1/\sqrt{(1-\beta^2)^2 + (2\xi\beta)^2}$ and $R(\xi, 0) = 1$.

Table A.1. Analytical expressions related to the transmissibility and the displacement response factor for a viscously damped SDOF system excited by a harmonic force considering both the classical and the new definitions

	Transmissibility	**Displacement response factor**
Classical definition	$\mathrm{TR_a}(\xi,\beta) = \sqrt{\dfrac{1+(2\xi\beta)^2}{(1-\beta^2)^2+(2\xi\beta)^2}} = \sqrt{1+(2\xi\beta)^2}\,R_{\mathrm{d}}(\xi,\beta)$	$R_{\mathrm{d}}(\xi,\beta) = \dfrac{1}{\sqrt{(1-\beta^2)^2+(2\xi\beta)^2}}$
	$\mathrm{TR_a}(\xi,0) = 1 \quad \forall\xi$	$R_{\mathrm{d}}(\xi,0) = 1 \quad \forall\xi$
	$\mathrm{TR_{a,max}}(\xi) = \dfrac{2\sqrt{2}\xi^2}{\sqrt{-1-4\xi^2+8\xi^4+\sqrt{1+8\xi^2}}}$	$R_{\mathrm{d,max}}(\xi) = \dfrac{1}{2\xi\sqrt{1-\xi^2}}$
	$\beta_{\mathrm{Ra}}(\xi) = \dfrac{1}{2\xi}\sqrt{-1+\sqrt{1+8\xi^2}}$	$\beta_{\mathrm{Rd}}(\xi) = \sqrt{1-2\xi^2}$
New definition	$\mathrm{TR}(\xi,\beta) = \dfrac{1}{2\sqrt{2}\xi^2}\sqrt{\dfrac{\left[1+(2\xi\beta)^2\right]\left(-1-4\xi^2+8\xi^4+\sqrt{1+8\xi^2}\right)}{(1-\beta^2)^2+(2\xi\beta)^2}}$	$R(\xi,\beta) = \dfrac{2\xi\sqrt{1-\xi^2}}{\sqrt{(1-\beta^2)^2+(2\xi\beta)^2}}$
	$\mathrm{TR}(\xi,0) = \dfrac{\sqrt{-1-4\xi^2+8\xi^4+\sqrt{1+8\xi^2}}}{2\sqrt{2}\xi^2} = \dfrac{1}{\mathrm{TR_{a,max}}(\xi)}$	$R(\xi,0) = 2\xi\sqrt{1-\xi^2} = \dfrac{1}{R_{\mathrm{d,max}}(\xi)}$
	$\mathrm{TR_{max}} = 1 \quad \forall\xi$	$R_{\mathrm{max}} = 1 \quad \forall\xi$

References

[1] I. G. Buckle, Passive control of structures for seismic loads, in: Proc. 12th World Conf. Earthq. Eng. No. 2834, Auckland, New Zealand, 2000, pp. 1–13. doi:10.1061/(ASCE)0733-9445(2008)134:1(3).

[2] R. A. Ibrahim, Recent advances in nonlinear passive vibration isolators, J. Sound Vib. 314 (3-5) (2008) 371–452. doi:10.1016/j.jsv.2008.01.014.

[3] M. Ismail, J. Rodellar, F. Pozo, Passive and hybrid mitigation of potential near-fault inner pounding of a self-braking seismic isolator, Soil Dyn. Earthq. Eng. 69 (2015) 233–250. doi:10.1016/j.soildyn.2014.10.019.

[4] R. S. Jangid, J. M. Kelly, Base isolation for near-fault motions, Earthq. Eng. Struct. Dyn. 30 (5) (2001) 691–707. doi:10.1002/eqe.31.

[5] J. M. Kelly, Earthquake-Resistant Design with Rubber, second edi Edition, Springer London, 1997.

[6] N. Menga, F. Bottiglione, G. Carbone, Nonlinear viscoelastic isolation for seismic vibration mitigation, Mech. Syst. Signal Process. 157 (2021) 107626. doi:10.1016/j.ymssp.2021.107626.

[7] I. G. Buckle, M. C. Constantinou, M. Diceli, H. Ghasemi, Seismic Isolation of Highway Bridges, Tech. rep., University of Buffalo, New York (2006).

[8] L. Di Sarno, Base Isolation of Railway Bridges, Int. J. Mech. 7 (3) (2013) 302–309.
[9] R. S. Jangid, Seismic Response of Isolated Bridges, J. Bridg. Eng. 9 (2) (2004) 156–166. doi:10.1061/(asce)1084-0702(2004)9:2(156).
[10] M. Kunde, R. Jangid, Seismic behavior of isolated bridges: A-state-of-the-art review, Electron. J. Struct. Eng. 3 (2) (2003) 140–169.
[11] J. Lopez Gimenez, T. Himeno, S. Yoshihara, A. S. M. Nuruzzaman, Seismic Isolation of Bridges: Devices, Common Practices in Japan, and Examples of Application, in: 4th Int. Conf. Adv. Civ. Eng., Vol. 2018, 2018, p. 6.
[12] V. A. Matsagar, R. S. Jangid, Seismic response of simply supported base-isolated bridge with different isolators, Int. J. Appl. Sci. Eng. 4 (1) (2006) 53–69.
[13] K. S. Park, H. J. Jung, I. W. Lee, A comparative study on aseismic performances of base isolation systems for multi-span continuous bridge, Eng. Struct. 24 (8) (2002) 1001–1013. doi:10.1016/S0141-0296(02)00020-2.
[14] K. Wilde, P. Gardoni, Y. Fujino, Base isolation system with shape memory alloy device for elevated highway bridges, Eng. Struct. 22 (3) (2000) 222–229. doi:10.1016/S0141-0296(98)00097-2.
[15] L. Casagrande, E. Villa, A. Nespoli, A. Occhiuzzi, A. Bonati, F. Auricchio, Innovative dampers as floor isolation systems for seismically-retrofit multi-storey critical facilities, Eng. Struct. 201 (2019) 109772. doi:10.1016/j.engstruct.2019.109772.
[16] A. S. Whittaker, M. Kumar, M. Kumar, Seismic isolation of nuclear power plants, Nucl. Eng. Technol. 46 (5) (2014) 569–580. doi:10.5516/NET.09.2014.715.
[17] C. Alhan, H. P. Gavin, Reliability of base isolation for the protection of critical equipment from earthquake hazards, Eng. Struct. 27 (9) (2005) 1435–1449. doi:10.1016/j.engstruct.2005.04.007.
[18] A. Chiozzi, M. Simoni, A. Tralli, Base isolation of heavy non-structural monolithic objects at the top of a masonry monumental construction, Mater. Struct. Constr. 49 (6) (2016) 2113–2130. doi:10.1617/s11527-015-0637-z.
[19] Y.-C. Fan, C.-H. Loh, J. N. Yang, P.-Y. Lin, Experimental performance evaluation of an equipment isolation using MR dampers, Earthq. Eng. Struct. Dyn. 38 (2009) 285–305. doi:10.1002/eqe.844.
[20] H. P. Gavin, A. Zaicenco, Performance and reliability of semi-active equipment isolation, J. Sound Vib. 306 (1-2) (2007) 74–90. doi:10.1016/j.jsv.2007.05.039.
[21] M. Hamidi, M. El Naggar, On the performance of SCF in seismic isolation of the interior equipment of buildings, Earthq. Eng. Struct. Dyn. 36 (2007) 1581–1604. doi:10.1002/eqe.708.
[22] M. Ismail, J. Rodellar, F. Ikhouane, An innovative isolation bearing for motion-sensitive equipment, J. Sound Vib. 326 (3-5) (2009) 503–521. doi:10.1016/j.jsv.2009.06.022.
[23] L. Y. Lu, G. L. Lin, Predictive control of smart isolation system for precision equipment subjected to near-fault earthquakes, Eng. Struct. 30 (11) (2008) 3045–3064. doi:10.1016/j.engstruct.2008.04.016.
[24] A. Reggio, M. De Angelis, Optimal design of an equipment isolation system with nonlinear hysteretic behavior, Earthq. Eng. Struct. Dyn. 42 (2013) 1907–1930. doi:10.1002/eqe.2304.
[25] A. Reggio, M. De Angelis, Combined primary-secondary system approach to the design of an equipment isolation system with High-Damping Rubber Bearings, J. Sound Vib. 333 (9) (2014) 2386–2403. doi:10.1016/j.jsv.2013.12.006.
[26] S. Taghavi, E. Miranda, Response Assessment of Nonstructural Building Elements, PEER Report 2003/05, 2003.
[27] I. Caliò, M. Marletta, Passive control of the seismic rocking response of art objects, Eng. Struct. 25 (8) (2003) 1009–1018. doi:10.1016/S0141-0296(03)00045-2.
[28] A. Contento, A. Di Egidio, Investigations into the benefits of base isolation for non-symmetric rigid blocks, Earthq. Eng. Struct. Dyn. 38 (2009) 849–866. doi:10.1002/eqe.870.
[29] S. Sorace, G. Terenzi, Seismic performance assessment and base-isolated floor protection of statues exhibited in museum halls, Bull. Earthq. Eng. 13 (6) (2015) 1873–1892. doi:10.1007/s10518-014-9680-3.
[30] M. Dicleli, S. Buddaram, Equivalent linear analysis of seismic-isolated bridges subjected to near-fault ground motions with forward rupture directivity effect, Eng. Struct. 29 (1) (2007) 21–32. doi:10.1016/j.engstruct.2006.04.004.
[31] S. A. Anagnostopoulos, Pounding of buildings in series during earthquakes, Earthq. Eng. Struct. Dyn. 16 (3) (1988) 443–456. doi:10.1002/eqe.4290160311.
[32] P. Komodromos, P. C. Polycarpou, L. Papaloizou, M. C. Phocas, Response of seismically isolated buildings considering poundings, Earthq. Eng. Struct. Dyn. 36 (12) (2007) 1605–1622. doi:10.1002/eqe.692.
[33] A. Masroor, G. Mosqueda, Experimental simulation of base-isolated buildings pounding against moat wall and effects on superstructure response, Earthq. Eng. Struct. Dyn. 41 (14) (2012) 2093–2109. doi:10.1002/eqe.2177.
[34] M. Papadrakakis, H. P. Mouzakis, Earthquake simulator testing of pounding between adjacent buildings, Earthq. Eng. Struct. Dyn. 24 (6) (1995) 811–834. doi:10.1002/eqe.4290240604.
[35] P. C. Polycarpou, P. Komodromos, On poundings of a seismically isolated building with adjacent structures during strong earthquakes, Earthq. Eng. Struct. Dyn. 39 (2010) 933–940. doi:10.1002/eqe.975.
[36] V. Crozet, I. Politopoulos, M. Yang, J. M. Martinez, S. Erlicher, Sensitivity analysis of pounding between adjacent structures, Earthq. Eng. Struct. Dyn. 47 (1) (2018) 219–235. doi:10.1002/eqe.2949.
[37] P. C. Polycarpou, P. Komodromos, A. C. Polycarpou, A nonlinear impact model for simulating the use of rubber shock absorbers for mitigating the effects of structural pounding during earthquakes, Earthq. Eng. Struct. Dyn. 42 (1) (2013) 81–100. doi:10.1002/eqe.2194.
[38] U. Andreaus, M. De Angelis, Influence of the characteristics of isolation and mitigation devices on the response of single-degree-of-freedom vibro-impact systems with two-sided bumpers and gaps via shaking table tests, Struct. Control Heal. Monit. 27 (5) (2020) 1–21. doi:10.1002/stc.2517.
[39] Y. Bao, T. C. Becker, T. Sone, H. Hamaguchi, Experimental study of the effect of restraining rim design on the extreme behavior of pendulum sliding bearings, Earthq. Eng. Struct. Dyn. 47 (4) (2018) 906–924. doi:10.1002/eqe.2997.
[40] P. S. Harvey, G.-P. Zéhil, H. P. Gavin, Experimental validation of a simplified model for rolling isolation systems, Earthq. Eng. Struct. Dyn. 43 (2014) 1067–1088. doi:10.1002/eqe.2387.
[41] P. S. Harvey, H. P. Gavin, Double rolling isolation systems: A mathematical model and experimental validation, Int. J. Non. Linear. Mech. 61 (2014) 80–92. doi:10.1016/j.ijnonlinmec.2014.01.011.

[42] P. S. Harvey, H. P. Gavin, Assessment of a rolling isolation system using reduced order structural models, Eng. Struct. 99 (2015) 708–725. doi:10.1016/j.engstruct.2015.05.022.
[43] M. Ismail, J. Rodellar, F. Ikhouane, An innovative isolation device for aseismic design, Eng. Struct. 32 (4) (2010) 1168–1183. doi:10.1016/j.engstruct.2009.12.043.
[44] M. Ismail, Inner pounding control of the RNC isolator and its impact on seismic isolation efficiency under near-fault earthquakes, Eng. Struct. 86 (2015) 99–121. doi:10.1016/j.engstruct.2014.12.041.
[45] M. Ismail, J. Rodellar, Experimental investigations of a rolling-based seismic isolation system, J. Vib. Control 24 (2) (2018) 323–342. doi:10.1177/1077546316640664.
[46] F. Peterka, Bifurcations and transition phenomena in an impact oscillator, Chaos, Solitons and Fractals 7 (10 SPEC. ISS.) (1996) 1635–1647. doi:10.1016/S0960-0779(96)00028-8.
[47] P. J. Christopher, B. Dobson, N. A. Alexander, Exploring the Dynamics of Base-Excited Structures Impacting a Rigid Stop, Math. Probl. Eng. 2020 (2020). doi:10.1155/2020/6721025.
[48] D. Costa, V. Vaziri, M. Kapitaniak, S. Kovacs, E. Pavlovskaia, M. A. Savi, M. Wiercigroch, Chaos in impact oscillators not in vain: Dynamics of new mass excited oscillator, Nonlinear Dyn. (2020). doi:10.1007/s11071-020-05644-0.
[49] M. Wiercigroch, S. Kovacs, S. Zhong, D. Costa, V. Vaziri, M. Kapitaniak, E. Pavlovskaia, Versatile mass excited impact oscillator, Nonlinear Dyn. 99 (1) (2020) 323–339. doi:10.1007/s11071-019-05368-w.
[50] H. Gritli, S. Belghith, Diversity in the nonlinear dynamic behavior of a one-degree-of-freedom impact mechanical oscillator under OGY-based state-feedback control law: Order, chaos and exhibition of the border-collision bifurcation, Mech. Mach. Theory 124 (2018) 1–41. doi:10.1016/j.mechmachtheory.2018.02.001.
[51] J. Ing, E. Pavlovskaia, M. Wiercigroch, Dynamics of a nearly symmetrical piecewise linear oscillator close to grazing incidence: Modelling and experimental verification, Nonlinear Dyn. 46 (3) (2006) 225–238. doi:10.1007/s11071-006-9045-9.
[52] M. Wiercigroch, V. W. Sin, Experimental study of a symmetrical plecewlse base-excited oscillator, J. Appl. Mech. Trans. ASME 65 (3) (1998) 657–663. doi:10.1115/1.2789108.
[53] G. W. Luo, X. H. Lv, Y. Q. Shi, Vibro-impact dynamics of a two-degree-of freedom periodically-forced system with a clearance: Diversity and parameter matching of periodic-impact motions, Int. J. Non. Linear. Mech. 65 (2014) 173–195. doi:10.1016/j.ijnonlinmec.2014.04.013.
[54] X. Lyu, Q. Gao, G. Luo, Dynamic characteristics of a mechanical impact oscillator with a clearance, Int. J. Mech. Sci. 178 (2020) 105605. doi:10.1016/j.ijmecsci.2020.105605.
[55] S. Yin, G. Wen, J. Ji, H. Xu, Novel two-parameter dynamics of impact oscillators near degenerate grazing points, Int. J. Non. Linear. Mech. 120 (2020) 103403. doi:10.1016/j.ijnonlinmec.2020.103403.
[56] G. Luo, L. Ma, X. Lv, Dynamic analysis and suppressing chaotic impacts of a two-degree-of-freedom oscillator with a clearance, Nonlinear Anal. Real World Appl. 10 (2) (2009) 756–778. doi:10.1016/j.nonrwa.2007.11.002.
[57] L. Wang, W. Xu, Y. Li, Impulsive control of a class of vibro-impact systems, Phys. Lett. Sect. A Gen. At. Solid State Phys. 372 (32) (2008) 5309–5313. doi:10.1016/j.physleta.2008.06.027.
[58] S. Lenci, G. Rega, A Procedure for Reducing the Chaotic Response Region in an Impact Mechanical System, Nonlinear Dyn. 15 (4) (1998) 391–409. doi:10.1023/A:1008209513877.
[59] Y. Liu, J. Páez Chávez, Controlling multistability in a vibro-impact capsule system, Nonlinear Dyn. 88 (2) (2017) 1289–1304. doi:10.1007/s11071-016-3310-3.
[60] Y. Liu, M. Wiercigroch, E. Pavlovskaia, Z. Peng, Forward and backward motion control of a vibro-impact capsule system, Int. J. Non. Linear. Mech. 70 (2015) 30–46. doi:10.1016/j.ijnonlinmec.2014.10.009.
[61] H. Gritli, Robust master-slave synchronization of chaos in a one-sided 1-DoF impact mechanical oscillator subject to parametric uncertainties and disturbances, Mech. Mach. Theory 142 (2019). doi:10.1016/j.mechmachtheory.2019.103610.
[62] F. Turki, H. Gritli, S. Belghith, Robust position control of a two-sided 1-dof impacting mechanical oscillator subject to an external persistent disturbance by means of a state-feedback controller, Complexity 2019 (2019) 18–22. doi:10.1155/2019/9174284.
[63] F. Turki, H. Gritli, S. Belghith, An LMI-based design of a robust state-feedback control for the master-slave tracking of an impact mechanical oscillator with double-side rigid constraints and subject to bounded-parametric uncertainty, Commun. Nonlinear Sci. Numer. Simul. 82 (2020) 1–26. doi:10.1016/j.cnsns.2019.105020.
[64] P. Brzeski, E. Pavlovskaia, T. Kapitaniak, P. Perlikowski, Controlling multistability in coupled systems with soft impacts, Int. J. Mech. Sci. 127 (2017) 118–129. doi:10.1016/j.ijmecsci.2016.12.022.
[65] X. Sun, H. Zhang, W. Meng, R. Zhang, K. Li, T. Peng, Primary resonance analysis and vibration suppression for the harmonically excited nonlinear suspension system using a pair of symmetric viscoelastic buffers, Nonlinear Dyn. 94 (2) (2018) 1243–1265. doi:10.1007/s11071-018-4421-9.
[66] Z. Hao, Q. Cao, M. Wiercigroch, Two-sided damping constraint control strategy for high-performance vibration isolation and end-stop impact protection, Nonlinear Dyn. 86 (4) (2016) 2129–2144. doi:10.1007/s11071-016-2685-5.
[67] Z. Hao, Q. Cao, The isolation characteristics of an archetypal dynamical model with stable-quasi-zero-stiffness, J. Sound Vib. 340 (2015) 61–79. doi:10.1016/j.jsv.2014.11.038.
[68] U. Andreaus, M. De Angelis, Nonlinear dynamic response of a base-excited SDOF oscillator with double-side unilateral constraints, Nonlinear Dyn. 84 (3) (2016) 1447–1467. doi:10.1007/s11071-015-2581-4.
[69] U. Andreaus, P. Baragatti, M. De Angelis, S. Perno, A Preliminary Experimental Study About Two-Sided Impacting SDOF Oscillator Under Harmonic Excitation, J. Comput. Nonlinear Dyn. 12 (6) (2017) 061010. doi:10.1115/1.4036816.
[70] U. Andreaus, P. Baragatti, M. De Angelis, S. Perno, Shaking table tests and numerical investigation of two-sided damping constraint for end-stop impact protection, Nonlinear Dyn. 90 (4) (2017) 2387–2421. doi:10.1007/s11071-017-3810-9.
[71] U. Andreaus, M. De Angelis, Experimental and numerical dynamic response of a SDOF vibro-impact system with double gaps and bumpers under harmonic excitation, Int. J. Dyn. Control 7 (4) (2019) 1278–1292. doi:10.1007/s40435-019-00532-x.
[72] G. Stefani, M. De Angelis, U. Andreaus, Scenarios in the experimental response of a vibro-impact single-degree-of-freedom system and numerical simulations, Nonlinear Dyn. 103 (4) (2021) 3465–3488. doi:10.1007/s11071-020-05791-4.

[73] G. Stefani, M. De Angelis, U. Andreaus, Numerical study on the response scenarios in a vibro-impact single-degree-of-freedom oscillator with two unilateral dissipative and deformable constraints, Commun. Nonlinear Sci. Numer. Simul. 99 (2021) 105818. doi:10.1016/j.cnsns.2021.105818.

[74] F. Naeim, J. M. Kelly, Design of Seismic Isolated Structures: From Theory to Practice, John Wiley, Chichester, U.K., 1999.

[75] G. Stefani, M. De Angelis, U. Andreaus, Influence of the gap size on the response of a single-degree-of-freedom vibro-impact system with two-sided constraints: experimental tests and numerical modeling, Int. J. Mech. Sci. 206 (2021) 106617. doi:10.1016/j.ijmecsci.2021.106617.

[76] K. J. Bathe, Finite Element Procedures, Prentice-Hall, Englewood Cliffs New Jersey, New York, 1996.

[77] M. Machado, P. Moreira, P. Flores, H. M. Lankarani, Compliant contact force models in multibody dynamics: Evolution of the Hertz contact theory, Mech. Mach. Theory 53 (2012) 99–121. doi:10.1016/j.mechmachtheory.2012.02.010.

[78] L. Skrinjar, J. Slavi, A review of continuous contact-force models in multibody dynamics, Int. J. Mech. Sci. 145 (2018) 171–187. doi:10.1016/j.ijmecsci.2018.07.010.

[79] P. Flores, M. Machado, M. T. Silva, J. M. Martins, On the continuous contact force models for soft materials in multibody dynamics, Multibody Syst. Dyn. 25 (2011) 357–375. doi:10.1007/s11044-010-9237-4.

[80] P. Flores, H. M. Lankarani, Contact Force Models for Multibody Dynamics, Springer, 2016.

[81] A. K. Chopra, Dynamic of Structures: Theory and Applications to Earthquake Engineering, 4th Edition, Pearson, Englewood Cliffs, New Jersey, 2012.

Highlights

- The occurrence of impact can significantly modify the response of SDOF systems.
- The study of the scenarios is functional to identify suitable control strategies.
- It is possible to exploit the occurrence of impact with beneficial effects.
- A unit value of the relaxation time allows to minimize the peak mass acceleration.
- Very small gaps involve an increasing reduction of the linear isolation frequency range.

CRediT Author Statement

Giulia Stefani: Software, Formal analysis, Investigation, Data Curation, Writing - Original Draft, Visualization. **Maurizio De Angelis:** Conceptualization, Validation, Writing - Review & Editing, Supervision, Funding acquisition. **Ugo Andreaus:** Validation, Writing - Review & Editing, Supervision, Funding acquisition.

Declaration of interests

☒ The authors declare that they have no known competing financial interests or personal relationships that could have appeared to influence the work reported in this paper.

☐The authors declare the following financial interests/personal relationships which may be considered as potential competing interests: